Complex and protracted environmental and ecological perturbations during OAE 1a - evidence from an expanded pelagic section from south Spain (Western Tethys)

J.M. Castro[1], G.A. de Gea[1], M.L. Quijano[2], R. Aguado[1], S. Froehner[3], B.D.A. Naafs[4] and R.D. Pancost[4]

1 Departamento de Geología and CEACTierra, Universidad de Jaén. E23071-Jaén, Spain. jmcastro@ujaen.es, raguado@ujaen.es, gadegea@ujaen.es

2 Departamento de Química Inorgánica y Orgánica and CEACTierra, Universidad de Jaén, Spain. lquijano@ujaen.es

3 Department of Environmental Engineering, Federal University of Parana, 81531-980, Curitiba-PR, Brazil, froehner@ufpr.br

4 Organic Geochemistry Unit, School of Chemistry, School of Earth Science, Cabot Institute for the Environment, University of Bristol, UK.

david.naafs@bristol.ac.uk, r.d.pancost@bristol.ac.uk

Abstract

The early Aptian Oceanic Anoxic Event (OAE) 1a represents a major perturbation in the global carbon cycle associated with significant environmental, biotic and sedimentary changes. The signature of this event is a global negative followed by a positive stable carbon isotope excursion (CIE), associated with the input of light-carbon into the climate system and subsequent widespread deposition of organic-rich sediments. This study uses biostratigraphy, C-isotope stratigraphy, biomarkers, and elemental geochemistry to stratigraphically and geochemically characterize OAE 1a at an expanded pelagic marine section from the western Tethys.

The high-resolution $\delta^{13}C_{org}$ analysis of the section highlights several successive negative CIEs during the onset of OAE 1a (isotope segment C3), pointing to rapid changes in global carbon cycling. The biomarker data indicate that the organic matter is thermally mature and is mainly of marine origin. The biomarker assemblage together with records of redox-sensitive trace elements suggest that sedimentation took place under generally well oxygenated waters punctuated by three short episodes of sea floor anoxia/dysoxia. The two first episodes of anoxia/dysoxia correlate with enhanced organic productivity during the main negative C-isotope excursion that represents the onset of the OAE 1a. They occurred at the final part of C-isotope negative excursions, likely as a response to C-release, increased temperatures and associated hydrological change and weathering, which resulted in increased fertilization-driven oxygen consumption. This was followed by the positive carbon isotope excursion, due to the burial of OM outpacing carbon input. The third episode of anoxia-dysoxia, which occurred later during the major positive C-isotope excursion, is not associated with fertilization, and perhaps instead reflects a general progressive depletion of oxygen during OAE 1a, linked to stagnation of marine waters. Interestingly, although the environmental parameters return to pre-OAE values at the end of the event, a biotic (especially microbial) perturbation persisted after OAE 1a. Our results suggest that instability in environmental conditions was the

main feature during OAE 1a in the western Tethys with notable changes extending from the onset to the post-OAE 1a interval.

KEYWORDS:

Oceanic anoxic event 1a, Aptian, Biomarkers, Trace Elements, Environmental perturbations

1. Introduction

Oceanic anoxic events (OAEs) represent marked changes in the state of the Earth System (Jenkyns, 2010), linked to major perturbations of the global carbon cycle that influenced both the marine and terrestrial realm (Skelton, 2003; Hay, 2017; Xu et al., 2017). The main sedimentary feature of OAEs is the deposition of widespread marine organic rich sediments (Schlanger and Jenkyns, 1976), although this deposition is not strictly synchronous (Jenkyns, 2010). OAEs have been considered as hyperthermal or hothouse episodes (Jenkyns, 2010, 2018; Kidder and Worsley, 2010; Foster et al., 2018), which are interpreted as geologically abrupt events of increased atmospheric CO_2, global warming, a C-isotope excursion and reduction in oceanic oxygen content, among their main features. High-resolution studies on the isotopic signature of OAEs have demonstrated that C-isotope stratigraphy, when combined with biostratigraphy, provides a robust correlation tool (Menegatti et al., 1998). OAEs are typically characterized by $\delta^{13}C$ anomalies, interpreted as the result of light carbon input and widespread deposition of organic matter and subsequent ^{12}C drawdown (e.g., Jarvis et al., 2011; Jenkyns, 2010).

The Early Aptian OAE 1a is one of the largest and is linked to environmental, biotic and sedimentary changes, that affected both marine and continental environments (e.g., Föllmi, 2012; Robinson et al., 2017). A distinctive feature of OAE 1a is the presence of a negative $\delta^{13}C$ excursion preceding the main positive isotope excursion (Menegatti et al., 1998). One of the first C-isotope stratigraphies of OAE 1a was based on the study of the Cismon and Rotter Sattel sections from the Alpine Tethys, leading to the definition of eight carbon segments (C1 to C8, Menegatti et al., 1998). These segments have been established as a standard for the early Aptian C-isotope stratigraphy and are used for stratigraphic correlation in sections worldwide; in the Tethys domain (Menegatti et al., 1998; Hochuli et al., 1999; Luciani et al., 2001; de Gea et al., 2003; Erba and Tremolada, 2004; Heimhofer et al., 2004; Aguado et al., 2008, 2014a, b; Li et al., 2008; de Gea et al., 2008b; Mehay et al., 2009; Millán et al., 2011, 2014; Najarro et al., 2011; Stein et al., 2011; Sánchez-Hernández and Maurrasse, 2016), in the Boreal domain (Gröcke et al., 1999; Föllmi et al., 2006; Mutterlose and Bottini, 2013), in the Pacific (Jenkyns, 1995; Ando et al., 2002; Price, 2003; Dumitrescu and Brassell, 2005), and Mexico (Bralower et al., 1999; Nuñez-Useche et al., 2015).

OAE 1a was originally defined as the interval C4 to the base of C7 (Menegatti et al., 1998). Recently most studies (e.g., Erba et al., 1999, 2010; Malinverno et al., 2010; Heldt et al., 2012; Aguado et al., 2014a, b; Mutterlose et al., 2014; Bottini et al., 2015; Naafs et al., 2016; Jenkyns, 2018) place the onset of the OAE 1a at the base of the negative shift (segment C3), where the first organic-rich black shales and first evidence of environmental change are recorded.

The most accepted trigger for OAE 1a is increased atmospheric CO_2 concentrations, derived from volcanogenic and/or methanogenic sources (e.g., Weissert and Erba, 2004; Mehay et al., 2009; Bottini et al., 2012; Erba et al., 2010, 2015; Naafs et al., 2016). Additionally, the intrusion of magma into organic-rich sediments has been also considered a source of CO_2 (Polteau et al., 2016). OAE 1a may have been triggered by the emplacement of the Ontong Java Plateau in the central Pacific Ocean (e.g., Erba, 1994; Larson and Erba, 1999; Jones and Jenkyns, 2001; Jenkyns, 2010). Perturbations in the Os isotope record (Tejada et al., 2009; Bottini et al., 2012) and pCO_2 reconstructions based on biomarkers (Méhay et al., 2009; Naafs et al., 2016) are consistent with C-input from such (submarine) volcanism during the onset of OAE 1a. A release of isotopically light carbon from partial methane hydrate dissociation might have played a minor role in the OAE1a (Méhay et al., 2009), and was likely not a major source of *p*CO2 during OAE 1a (Naafs et al., 2016).

Elevated pCO_2 led to global warming (Beerling and Rogers, 2002; Ando et al. 2008; Tejada et al., 2009; Mehay et al., 2009; Mutterlose et al., 2014; Bottini et al., 2015; Naafs and Pancost, 2016) and a subsequent activation of the hydrological cycle, causing an increased nutrient influx to the ocean due to higher weathering rates (Kump et al., 2000; Jenkyns, 2010; Blättler et al., 2011). Many studies have documented an increase in surface-water fertility accompanied by high primary productivity (e.g., Aguado et al., 2014a; Bottini et al., 2015). The key feature of the sedimentary record of OAE 1a, and OAEs in general, is the widespread accumulation of organic-rich marine deposits (e.g. Jenkyns, 2010). Extensive accumulation of organic matter in marine environments has been classically linked to enhanced productivity and/or enhanced preservation, being the last related to low oxygen concentrations (Demaison and Moore, 1980; Pedersen and Calvert, 1990; Tyson, 2001, 2005). The discussion about the relative roles of both factors has been the origin of controversies, with the balance now tipping in favor of the productivity as generally the more important factor during OAEs (Jenkyns, 2010; Westermann et al., 2013; Aguado et al., 2014), although a combination of both origins is not mutually exclusive. As plankton productivity increases the oxygen-minimum zone intensifies, in a positive feedback mechanism (Jenkyns 2003). Other carbon-rich sediments, as sapropels (e.g., Martínez-Ruiz et al., 2015) are similarly explained. Evidence from multiple independent organic and inorganic proxies is crucial to shed light into this controversy, and is the aim of this study.

Detailed high-resolution studies show that, besides the general long-term environmental perturbations across OAE 1a, rapid changes also occurred, pointing to a complex evolution during this event, with variations in redox conditions (e.g., Westermann et al., 2013) or in temperatures (e.g., Dumitrescu et al 2006; Bottini et al., 2015; Naafs and Pancost, 2016; Jenkyns 2018). In this context, new high-resolution records enhancing the database of stratigraphy, chemostratigraphy and biostratigraphy are crucial to establish the time and cause-effect relationships between the long and short-term environmental changes, their causes and feedbacks, and the consequences in the biota. These will contribute to unravelling the complex processes involved in this global perturbation of the carbon cycle, ultimately increasing our understanding on the dynamics of Earth's system in a greenhouse world (Hay, 2017).

Here we document an expanded pelagic succession from the western Tethys, the Carbonero section in S. Spain. We use high-resolution C-isotope stratigraphy and a combination of elemental and organic geochemistry to explore changes in environmental conditions at this site and their impact in the biota. The aim of this study is to present a high-resolution record of the early Aptian OAE 1a, adding a new correlation section to the global database. We also provide a new detailed reconstruction of the environmental changes recorded in a western Tethys pelagic basin across OAE 1a, allowing us to explore further aspects of local vs. global change in productivity and anoxia, and their impact on marine ecosystems. This study aims to contribute to the knowledge of the functioning of the Earth System during hyperthermals, which has a further interest as they are considered as analogues to present and future climate change.

2. Location and geological background

The Carbonero section is located in the Jaén province, Southeast Spain, in the site named Solana de Morales (geographic coordinates: base, 37° 33' 39.40"N, 3° 48' 2.27"W; top, 37° 33' 41.85"N, 3° 48' 4.08"W) (Fig. 1A). This section belongs to the Subbetic Zone of the External Zones of the Betic Cordillera (EZBCs), which comprises sedimentary successions deposited in the South Iberian Palaeomargin (SIP) during the Alpine tectonic cycle (Triassic to the early Miocene, see Fig. 1B). The Lower Cretaceous sequence of the SIP includes thick successions (> 3000 m) of carbonates and siliciclastics that were deposited on shallow platforms (mostly in the so-called Prebetic Zone, Fig. 1C) and hemipelagic/pelagic settings (dominant in the Subbetic Zone, Fig. 1C) (e.g., Ruiz-Ortiz, 1980; Martín-Chivelet et al., 2002; Vera, 2004). At present, the Subbetic is a major tectonic unit of the EZBCs, composed of several thrusts with a general SW–NE strike, made of mostly Mesozoic pelagic successions. The Subbetic Zone is an allochthonous tectonic unit that thrusts over the Prebetic Zone, a para-autochthonous unit made of shallow-marine sedimentary successions with intercalations of continental facies, that represents the northern part of the EZBCs.

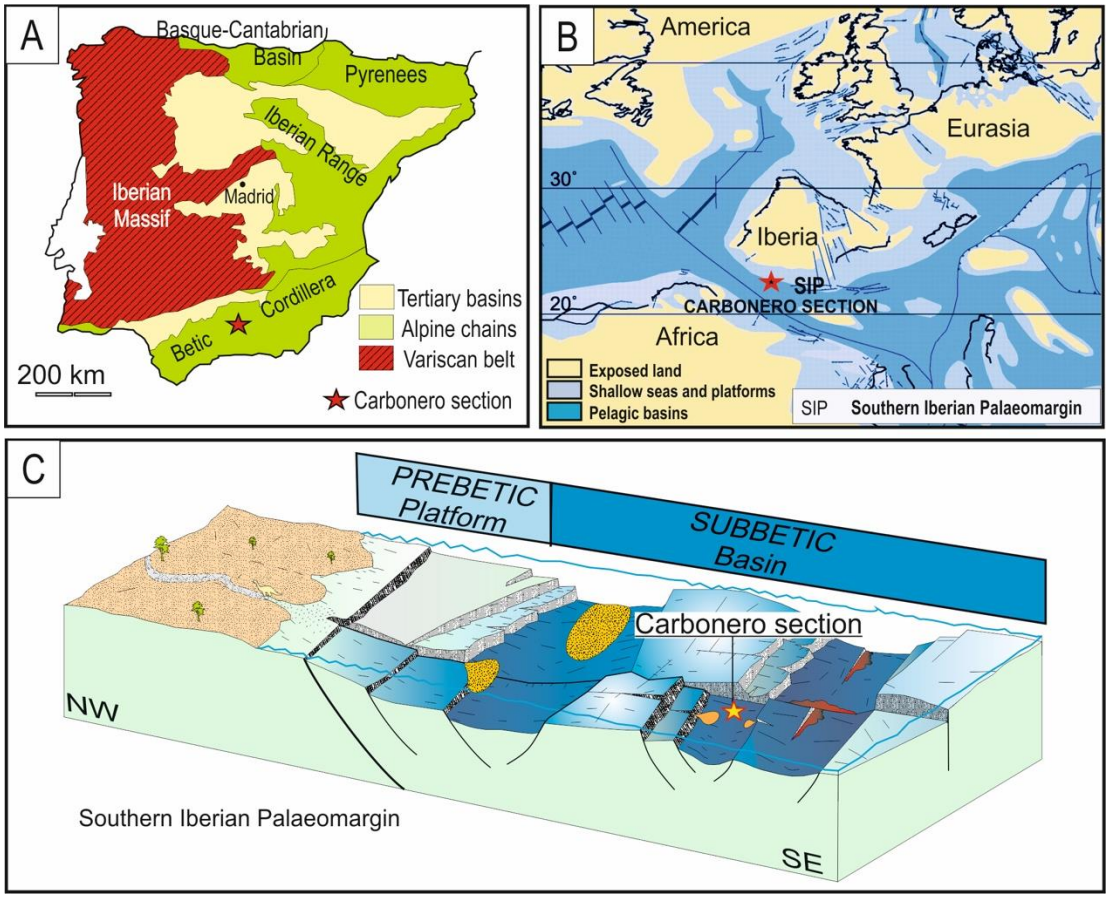

FIGURE. 1. A. Current location of the Carbonero section in the central part of the Betic Cordillera, southern Spain. B. Early Aptian (~120 Ma) palaeogeographic reconstruction of the western Tethys (simplified from Masse et al., 2000) showing the location of the Carbonero section in the Southern Iberian Palaeomargin (SIP). C. Reconstruction of the SIP during the Early Aptian (modified from de Gea et al., 2008b).

2.1. Palaeogeography and palaeoclimates

During the Early Cretaceous, the Carbonero section was located in the northwestern corner of the Tethys (Fig. 1B). The configuration of the SIP was defined by a series of basin-scale troughs and swells, bounded by large extensional faults roughly parallel to the continental margin, that were initiated in the Middle Jurassic (Fig. 1C) (e.g., Azéma et al., 1979; García Hernández et al., 1980; Vera, 1988; Ruiz-Ortiz et al., 2001). This tectonic pattern controlled strong lateral changes in subsidence, deposition rates and facies. During the Aptian, the SIP was strongly influenced by the relative motions of the contiguous Eurasian and African plates (Fig. 1B). Initiation of the seafloor spreading in the North Atlantic that started very early in the Cretaceous, led to a reversion in the sinistral movement between Iberia and Africa that had prevailed during part of the Jurassic (Ziegler, 1988). It started a phase of anti- clockwise rotation of Iberia relative to Europe, linked

to the opening of the Bay of Biscay from the middle Aptian onwards (Olivet, 1996; Vergès and García-Senz, 2001). In that geodynamic framework, extensional tectonics prevailed in the SIP.

The onset of the Aptian was marked by a pulse in extensional tectonics, triggering the formation of tilted blocks that resulted in notable lateral changes in subsidence rates, with highly subsident sectors surrounded by low subsident and even uplifting sectors, controlled by listric faults (e.g., Martín-Chivelet et al., 2002; Vilas et al., 2003; Vera, 2004). De Gea et al. (2008a) provided a detailed study of several sections within the area and proposed a model of a small subsiding pelagic sub-basin bounded by active faults leading to scarps feeding the turbidite levels, associated with volcanic activity (Fig. 1C). This small sub-basin has a thicker and more complete stratigraphic record than the surrounding areas, specifically during the early Aptian, (Molina, 1987; Aguado et al., 1993; Molina and Hernández-Molina, 1993; de Gea et al., 2008). A palaeolatitude of 20º–25º N has been inferred from the Aptian position of the section (e.g., Masse et al., 1993) (Fig. 1B). According to the palaeoclimatic reconstructions of Chumakov et al. (1995), during the Aptian, the studied section was located in the northern part of the equatorial arid belt, close to the boundary with the mid-latitude warm humid belt. Palaeoclimatic reconstructions from a nearby section (La Frontera section, Aguado et al., 2014a), show interesting changes towards more humid conditions across OAE 1a that could be explained by a southward expansion of the humid climate belt during the early Aptian.

2.2. Stratigraphy, sedimentology and biostratigraphy

The stratigraphic succession of the Carbonero section mainly belongs to the Carbonero Formation (Molina, 1987) within the Ventisquero-Sierra del Trigo tectonic unit (Sanz de Galdeano, 1973). The Carbonero Formation lies on the marly limestones and grey marlstones (Berriasian–Barremian) of the Carretero Formation (de Gea, 2004; de Gea et al., 2008b). Its top is not preserved due to faulting or localized erosion. The Carbonero Formation represents one of the most complete records of Aptian sedimentation in the External Zones of the Betic Cordillera (de Gea et al., 2008b), which laterally correlates with large hiatuses throughout the Subbetic Zone (Vera, 2004). Detailed stratigraphic and sedimentological characterizations of this formation can be found in Molina (1987), Molina et al. (2001), de Gea (2004) and de Gea et al. (2008b).

The Carbonero section (Fig. 2) was originally proposed as the stratotype of the Carbonero Formation (Molina, 1987), and the present study focuses on the interval equivalent to its lower ~82 m. Three members, designated as lower, middle and upper, were initially distinguished. The lower member (~18 m thick) lies on an unconformity at the top of the marlstones and marly limestones of the Carretero Formation, and comprises a pebbly mudstone at the base, overlaid by

bluish-grey marlstones with several intercalations of calcareous turbidites and some barite concretions. The middle member has a thickness of ~46 m and is composed of marlstones, black shales, dark clayey marlstones, and dark brown radiolarite beds interbedded with dark siliceous shales. Some levels of fine-grained volcanoclastic rocks (cinerites) are intercalated within the dark marlstones at about 30–32 m (Fig. 2). Two horizons of carbonate concretions are present at ~45 m and ~51.5 m. The studied part of the upper member is ~16 m thick and comprises an alternation of light-green marlstones and calcarenites. Previous studies (de Gea et al., 2008a, b, c; O'Dogherty et al., 2011; Quijano et al., 2012; Aguado et al., 2014a, b) indicate that most of the sedimentary record of the middle member of the Carbonero formation represents the local expression of the OAE 1a.

Biostratigraphic analysis of the Carbonero section is based mainly on calcareous nannofossils (Aguado et al., 1993; Aguado, 1994; de Gea, 2004; de Gea et al., 2008a, c) although some radiolarian data also exist (Aguado et al., 1993; O'Dogherty, 1994). Contrary to other outcrops of the Carbonero Formation (Aguado et al., 2014a, b), calcareous microfossils at Solana de Morales are only moderately preserved or absent. Moderately preserved calcareous nannofossil assemblages were found through the lower (~0 m to ~36 m) and uppermost (~68 to ~82 m) parts of the section but are absent through the radiolaritic interval (~36 m to ~52 m) and very poorly preserved in the black shales above the radiolarites (~52 to ~65 m). The first record (FR) of *Hayesites irregularis*, the FR of *Eprolithus floralis* and the last record (LR) of *Conusphaera rothii* (Fig. 2) allowed the identification of the NC5 (part), NC6A, NC6B and NC7 (part) zones of Bralower et al. (1995). The LR of *C. rothii* and the FR of *E. floralis* probably do not correspond with their respective true last and first occurrences, due to the presence of intervals with absence of a calcareous nannofossil record or poorly preserved assemblages linked to low carbonate content (Fig. 2). The onset of the 'nannoconid crisis' event was also recorded at ~20 m. Two small hiatuses were identified by means of biostratigraphy (see de Gea et al., 2008b for details): the first is linked to the unconformity at the base of the Carbonero formation and the second is located at ~20 m, coinciding with the onset of the 'nannoconid crisis' (Fig. 2). The main radiolaritic interval (~36 m to ~52 m) remains unzoned.

3. Methods

3.1. Fieldwork and sampling

The Solana de Morales section was re-measured and sampled, with a total of 140 samples taken for bulk geochemical analyses, at an average of 0.6 metres intervals from a total measured thickness of 80 m. Of these, 34 samples at an average of 2.5 meters interval were selected for biomarker analysis, and 47 samples for elemental geochemistry and TOC analyses. Samples for biomarker analyses were packed in aluminium foil in order to avoid contamination from plastics.

190

191 *3.2. C and O isotopes*

192 Bulk C- and O-isotope analyses of the carbonate fraction ($^{13}C_{carb}$) of all the collected samples were carried out at the Stable
193 Isotope Laboratory of the University of Michigan, using a Finnigan MAT Kiel IV preparation device coupled directly to the
194 inlet of a Finnigan MAT 253 triple-collector isotope ratio mass spectrometer. The international carbonate standard NBS-
195 19 was used to calibrate to Vienna PeeDee Belemnite (VPDB), with an average precision of 0.15‰. The C-isotope analyses
196 of the total organic fraction ($^{13}C_{org}$) of all the collected samples were performed at the Stable Isotope Laboratory (SIDI) of
197 the Universidad Autónoma of Madrid. Samples were treated with 3% HCl for 24 h to remove carbonates and then analysed
198 with a Carlo Erba 1108 elemental analyser coupled to an IRMS VG Isochrom in continuous flow mode. The results were
199 calibrated to the VPDB standard, with a precision better than 0.1‰.

200

201 *3.3. Elemental geochemistry and TOC*

202 34 samples were selected for determination of total organic carbon (TOC) contents. The analyses were performed in the
203 Microanalytical Laboratory at the University of Bristol using a Coulomat 702 Analyser for coulometric determination of
204 Total Carbon and Inorganic Carbon and Eurovector EA3000 Elemental Analyser for nitrogen analyses. The TOC
205 concentration was determined by subtracting the inorganic carbon (IC) concentration from the total carbon (TC) in each
206 sample. A selection of 47 samples was analysed for major and trace elements. Powdered samples were dried at 40°C during
207 24 h and later, 100 mg of sample was acid digested in closed PTFE vessels with a combination of $HNO^{3+}HF^{+}$ $HClO^{4}$ (2.5 ml:
208 5 ml: 2.5 ml v/v). The samples were evaporated and, 1 ml of HNO_3 was added to make a double evaporation. Finally, the
209 sample was re-dissolved and diluted with MilliQ water (18.2 $M\Omega cm^{-1}$) and 1 ml of HNO_3 in a 100 ml volume flask. Analysis
210 were performed using a high resolution inductively coupled plasma-mass spectrometry (HR-ICP-MS, Thermo Scientific,
211 model Element XR). In order to improve the sensitivity of the ICP-MS, a tuning solution containing 1 $\mu g.l^{-1}$ Li, B, Na, K, Sc,
212 Fe, Co, Cu, Ga, Y, Rh, In, Ba, Tl, U was used, and as internal standard, 20 $mg.l^{-1}$ of a monoelemental solution of ^{115}In. The
213 detection limit (DL) was calculated as three times the standard deviation of the average of 10 blanks. The precision of the
214 results was expressed in terms of 2 standard deviation of a set of 8 reference materials measurements. The value of
215 accuracy (%) was calculated using the absolute value of the difference between the measured values obtained during the
216 analysis and the certified values of a set of 8 reference materials analysis. Several commercial solutions were used in order
217 to perform the different calibration curves. These analyses were performed in the Geotop Laboratory of the Institute of

Earth Sciences Jaume Almera (Barcelona). Elemental concentrations are expressed as normalized values with respect to Al in order to compensate for the dilution effect (Calvert and Pedersen, 2007).

3.4. Organic geochemistry

Initial processing of samples was carried out in the University of Jaén. Bulk rock samples were cleaned with dichloromethane:methanol (DCM:MeOH) 2:1 to remove any contamination from handling. Then samples were coarsely crushed into small pieces (approximately 1 cm) using a mortar and subsequently finely crushed using a ball mill (pre-rinsed with dichloromethane and acetone) at under 400 rpm for 12 minutes. The organic geochemical analyses were performed at the Organic Geochemistry Unit, University of Bristol. The finely ground samples (~30 g) were extracted for 24 h into 200 mL of dichloromethane:methanol azeotrope (8:2, v/v; containing activated copper turnings to remove elemental sulphur) using a Soxhlet apparatus. After extraction, the turnings were removed and the samples were concentrated using rotary-evaporation under reduced pressure and dried through a column of sodium sulphate. Total lipid extracts were then separated by flash column chromatography using silica gel and sequential elution with hexane, hexane:dichloromethane (9:1, v/v) and methanol, yielding three fractions containing saturated hydrocarbons, aromatic hydrocarbons, and polar compounds, respectively. The saturated hydrocarbon (containing *n*-alkanes, steranes, and hopanes) and aromatic fractions were analysed by gas chromatography–mass spectrometry (GC–MS) on a Thermo DSQ II gas chromatograph connected to a Thermo Trace Ultra GC–MS. The analytical procedures followed the method described by Quijano et al. (2012). Biomarkers were identified by comparison with published mass spectra and retention times.

4. Results

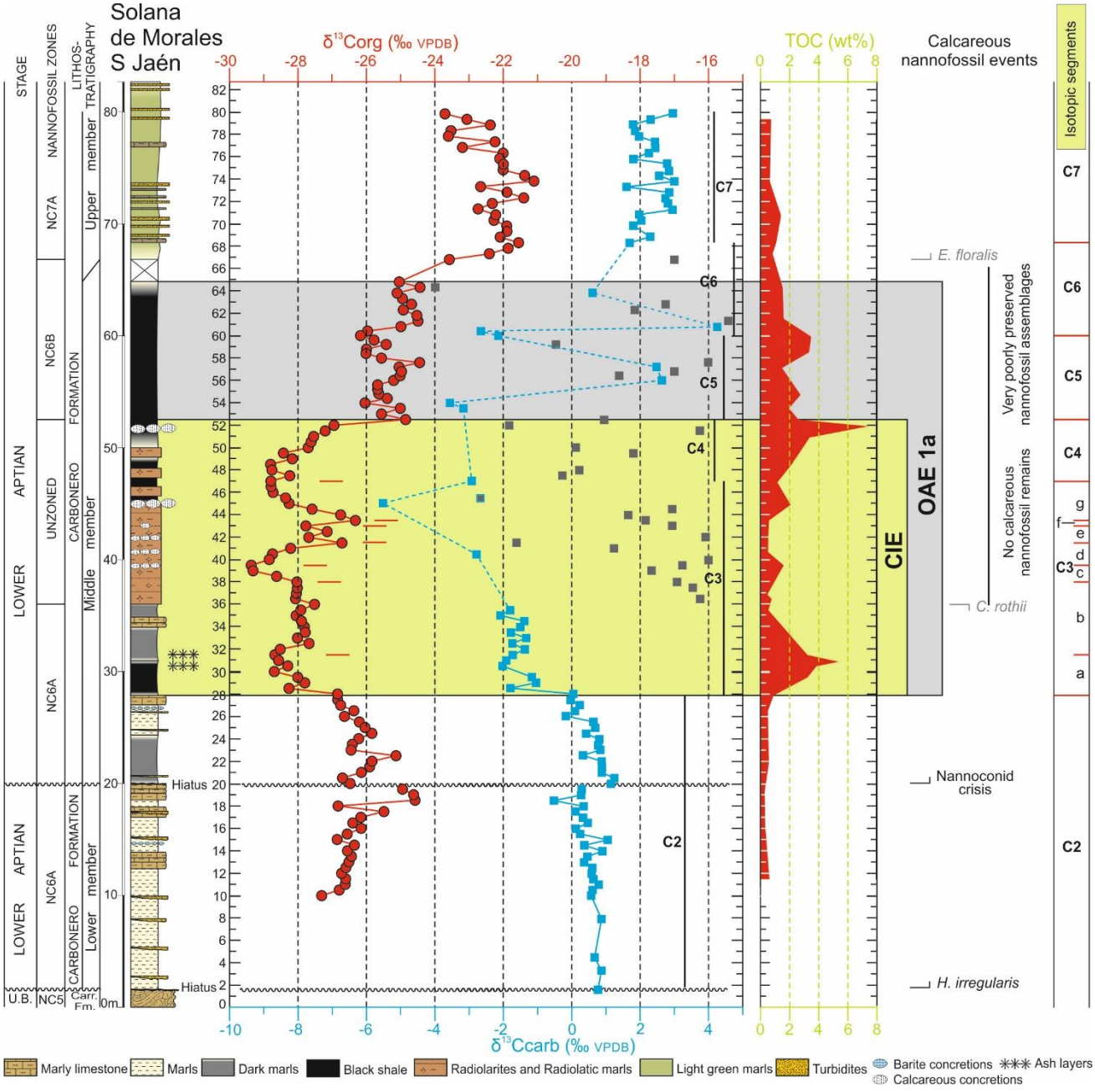

238

239 FIGURE. 2. Lithologic column, lithostratigraphical units and calcareous nannofossil biostratigraphy for the Carbonero
240 section. Calcareous nannofossil zones are after Roth (1978) and Bralower et al. (1995). Stable C-isotope geochemistry
241 ($\delta^{13}C_{org}$ and $\delta^{13}C_{car}$ curves), total organic carbon (TOC) and main biostratigraphic events are also presented. Grey dots
242 represent not reliable $\delta^{13}C_{carb}$ values due to very low carbonate content. The Menegatti et al. (1998) segments (C2–C7) are
243 indicated in the C-isotope curves. Red arrows within the C3 segment of the $\delta^{13}C_{org}$ curve indicate minor shifts used to
244 differentiate a–g subsegments shown on the right side. The shaded bands correspond to the negative C-isotope excursion
245 (CIE) and OAE 1a interval. Abbreviations for calcareous nannofossil taxa: *H. irregularis* = *Hayesites irregularis*; *N. truittii* =
246 *Nannoconus truittii*; *C. rothii* = *Conusphaera rothii*; *E. floralis* = *Eprolithus floralis*.

4.1. C-isotope stratigraphy

The $\delta^{13}C_{org}$ profile displays a distinctive evolution, with a lower part (10 m to 28 m) with relatively stable values of around -27‰, followed by a broad negative excursion (2-3‰) between ~28 m and 52 m with several successive negative peaks (minima around -29‰). The profile continues with a 2-step positive excursion, reaching around -25‰ in the first step (52.5 to 65 m) and maxima of -22 to -21‰ in the second step (65 to 78 m), and finishes with a slight decreasing trend towards ~ -24‰ at the top (Fig. 2).

The low abundance of carbonate during most of OAE 1a (~36-68 m) precludes us from generating a reliable high-resolution $\delta^{13}C_{carb}$ record. Throughout the intermediate interval (35.5 m–68 m), the obtained $\delta^{13}C_{carb}$ values have an erratic distribution due to extremely low carbonate content of most samples (< 1 %) (grey square dots in Fig. 2). The $\delta^{13}C_{carb}$ profile, excluding this intermediate interval, mimics the main fluctuations observed in the $\delta^{13}C_{org}$ profile, ranging from ~2 to -4‰, with a negative and subsequently positive CIE.

4.2. Elemental geochemistry

Total organic carbon (TOC) fluctuates from 0.2 to 7 wt.%, reaching the highest values at ~52 m. Two other intervals with maximum TOC values (> 2%) occur at *i*) ~29 m to ~35 m, located below the radiolaritic interval, reaching maximum values of 5.1% and *ii*) at 60 m, reaching a maximum of 3.2%. TOC values < 1% characterize the interval equivalent to the radiolaritic facies (Fig. 2).

Abundances of major and trace elements were measured in order to reconstruct changes in the redox conditions, productivity, and terrestrial fluxes. Normalized concentrations are compared to the average shale value (ASV) (Wedepohl, 1991; Brumsack, 2006) to estimate level of enrichment or depletion of the analysed elements. Proxies for productivity (TOC, Ba/Al, P/Al), continental sources (Rb/Al, Mg/Al, K/Al, Ti/Al, and Zr/Al), and redox conditions (U/Th, Ni/Co, V/Cr, V/Al, U/Al, Cr/Al and V/Sc) are presented in Fig. 3. Ba/Al and P/Al ratios exhibit more highly variable vertical evolution, with Ba/Al well above the ASV, and P/Al generally below. There is a consistency in the two indices and TOC contents, with all three exhibiting two maxima at 30 m and 51 m. However, a third maximum in TOC (at 58.6 m) corresponds with minima in Ba/Al and P/Al (Fig. 3). The elements selected as proxies for continental sources record high variability through the section, with values generally above the AVS (Rb/Al, K/Al and Ti/Al), or in average within the AVS (Mg/Al and Zr/Al). Collectively, they show a minimum at 28 m, and three maxima at 30–32 m, 49.5–52 m and 61-67 m. Another less pronounced peak is located at 44.5 m (Fig. 3). Redox sensitive trace elements (RSTE) are presented as Al-normalized abundances, as well as the U/Th,

Ni/Co and V/Cr indices proposed by Jones and Manning (1994), and the V/Sc index (Kimura and Wanatabe, 1991). All of the profiles (Fig. 3) show a marked variability through the section, with generally parallel trends, with the exception of the lowermost part of the section. Three maxima are depicted in all indices, at 30–32.5 m, 49.5–52.5 m and 57.6–61.3 m (except Cr/Al at 57.6–61.3 m) (Fig. 3). Another smaller maximum occurs from 39.5 to 43.5 in most indices (except U/Th and Ni/Co).

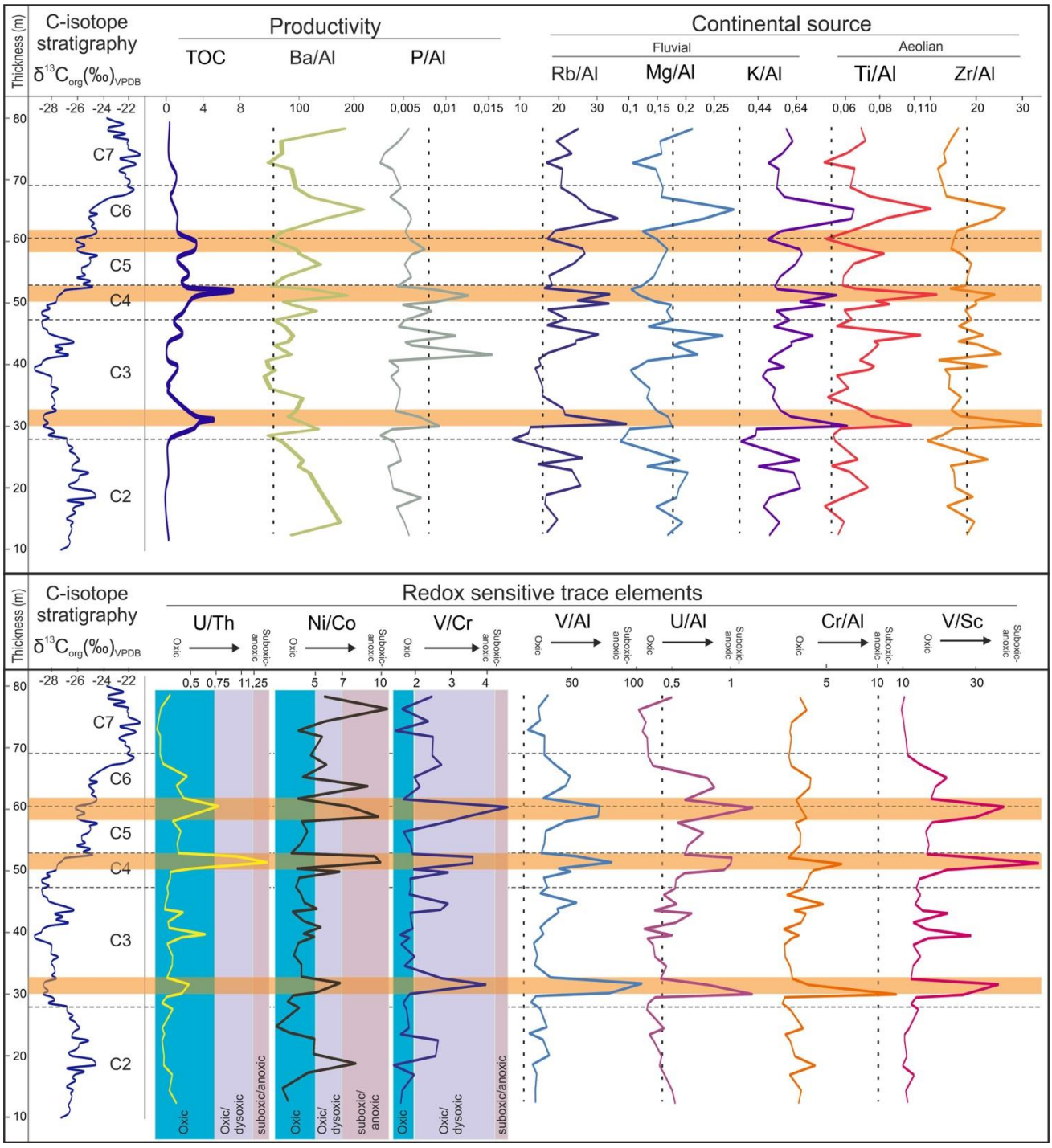

FIGURE 3. Stratigraphic distributions of selected elements and elemental ratios. U/Th, Ni/Co and V/Cr indices are plotted following the different oxygen-content zones according to Jones and Manning (1994). Values for Al-normalized elements correspond to Element/Al for major elements and Element/Al x 10^{-4} ppm for trace elements. Dashed lines in Al-normalized profiles represent values of the average shale (Wedepohl, 1991; Brumsack, 2006).

4.3. Organic geochemistry

The saturated hydrocarbon fraction is dominated by *n*-alkanes, acyclic isoprenoids, steranes and hopanes, although some samples also contain high-molecular-weight unresolved complex mixtures (UCM).

4.2.1. *n*-Alkanes

The *n*-alkanes are the dominant compounds in most chromatograms, with the *n*-C_{13} to *n*-C_{35} homologues being present in most samples. Short chain low-molecular-weight (LMW) components are dominant, with the *n*-C_{17} to *n*-C_{21} compounds being the most abundant. To facilitate interpretation of these *n*-alkane distributions, we calculated two different ratios: the HMW/LMW ratio ([*n*-C25 + *n*-C26 + *n*-C27 + *n*-C28 + *n*-C29]/[*n*-C17 + *n*-C18 + *n*-C19 + *n*-C20 + *n*-C21]) in order to constrain the relationship between long and short-chain compounds (Fig. 4); and the carbon preference index (CPI), to obtain an estimate of the thermal maturity (Bray and Evans, 1961). The average HMW/LMW ratio is 0.4 ± 0.1 (Fig. 4), but high variability occurs through the section. It generally decreases from 22 m (0.77) to 52 m (0.24), followed by an increasing trend towards the top (0.52). Imposed on these trends are maxima at 22 m (0.77), 40.8 m (0.54), 53.5 m (0.63) and 73.8 m (0.55) (Fig. 4). The CPI ratio has average values of 1.2, with lower values (1.15) during C3 to C5 C-isotope segments, and higher values within the C2 (1.32) and C6-C7 (1.36) segments. These are consistent with thermally mature organic matter.

4.2.2. Isoprenoids

Pristane and phytane, likely derived from the degradation of the phytyl side-chain of chlorophyll, are abundant in all samples and their abundances exhibit high variability through the section. Pr/Ph ratios range from 1.7 to 5.5, with average values of 2.9 ± 0.8. Values have maxima at 19.25 m and 68.3 m, whereas within the middle interval (37–67 m) values are lower (Fig. 4). The isoprenoids/*n*-alkane ratios were plotted following the classic diagram of Didyck et al (1978) (Fig. 4) in order to infer redox conditions, noting the many caveats associated with this approach (discussed below). Pr/*n*-C_{17} ratios range between 0.7–2.0, whereas Ph/*n*-C_{18} ratios are higher but with a similar range of values, between 2–3.2 (Fig. 5).

4.2.3. Hopanes

Hopanes, the diagenetic and catagenetic products of biohopanoids from diverse bacteria, are present in all samples. There is a marked increase in relative abundance in the uppermost part of the section. They have a typical, thermally mature distribution, ranging in carbon number from C_{27} to C_{35}, with the C_{30} hopane being the dominant homologue. 17α,21β(H) hopanes are dominant over the 17β,21α(H) hopanes, and hopanoids with the biological 17β,21β(H) configuration are absent. The C_{31}-C_{35} hopanes show the commonly observed decrease in abundance with increasing carbon chain. Other hopanoids present in all samples are the C_{31} 2-methylhopanes. In order to analyse stratigraphic trends in the hopane distributions, several ratios were calculated:

(1) The 22S/(22S+22R) homohopane ratio. These ratios are stable through the section, with values of 0.58 and a standard deviation of 0.02, indicative of high thermal maturity.

(2) The C_{30} βα/(βα + αβ) hopane ratio, has an average value of 0.2 (mature organic matter) and its depth profile is characterized by a marked increase from 58 m upwards to ~0.4 (Fig. 4).

(3) The C_{31} 2-Me-hopane index, 100 x C_{31} 2-MeHop/(C_{31} 2-MeHop + C_{31} Hop) (Summons et al., 1999), ranged from 2 to 25%, with three prominent peaks, at 30.5 m, 37 m and 54.8 m (Fig. 4).

(4) The redox sensitive Homohopane index (HHI: the ratio of 100 x C_{35}/(C_{31} + C_{35}) hopanes, Bishop and Farrimond, 1995; Peters et al., 2005), is generally low but varies between 1% and 10%, with three peaks above 8% at 31 m, 52.4 m and 60 m (Fig. 4).

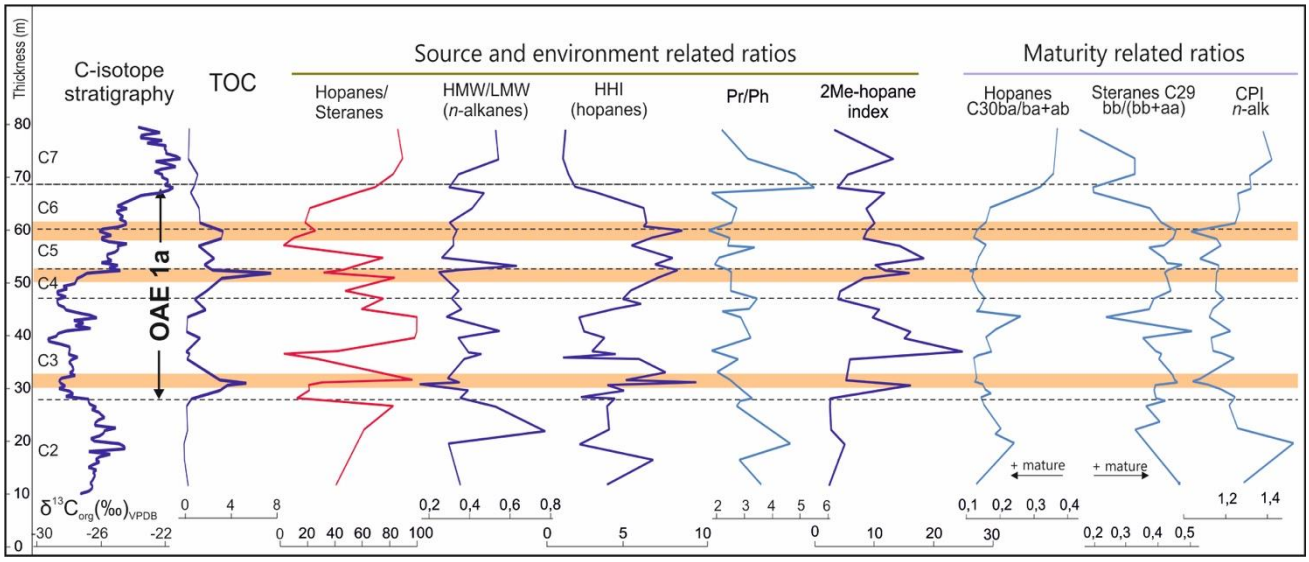

FIGURE 4. Biomarker ratios selected as proxies for source and environmental reconstructions and thermal maturity plotted against C-isotope stratigraphy. See explanation in text.

4.2.4. Steranes

A range of C_{27} to C_{29} steranes, derived from alteration of sterols from eukaryotes, are found in all samples. The relative distributions are similar, with C_{29} always being dominant (42–58%), but proportions of C_{29} and C_{27} increase and hose of C_{28} sterane decrease in the upper part of the section, from 56.8 m upwards. The regular sterane diastereomers are represented by the four epimers (5α(H),14α(H),17α(H),20R; 5α(H),14α(H),17α(H),20S; 5α(H),14β(H),17β(H),20S and 5α(H),14β(H),17β(H),20R), which are all abundant, with vertical variations in their relative abundance. Furthermore, 13β,17α steranes (diasteranes) are relatively abundant compared to regular steranes. In order to investigate the vertical variations in the sterane distributions sensitive to thermal maturity we have calculated the C_{29} ββ/(ββ+αα) ratio, which has an average value of 0.4 from the base up to 60 m, and then decreases to a minimum of 0.2 around at 70 m with an average of 0.25 in the interval 60–79 m (Fig. 4). The C_{29} 20S/(20S+20R) sterane ratio has stable values around 0.5 across the section, consistent with high thermal maturity. In order to assess the relative proportions of steranes and hopanes, we calculated the ratio of total hopanes to total steranes (Hopanes/Steranes = $C_{27\text{-}29}$ steranes/ $C_{27\text{-}29}$ steranes + $C_{27\text{-}35}$ hopanes) (Fig. 4).

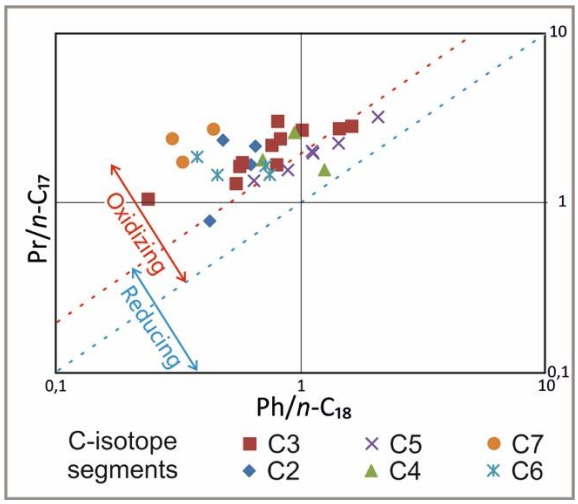

FIGURE 5. Pr/*n*-C_{17} *vs*. Ph/*n*-C_{18} plot. Samples from the C2 to C7 C-isotope segments are marked. The reference lines are from Didyck et al., 1978.

5. Discussion

5.1 C-isotope stratigraphy and correlation

Due to the very low proportion of carbonate, the $\delta^{13}C_{carb}$ curve has a poor resolution throughout most of the middle member of the Carbonero Formation (~35-70 m) in the Carbonero section. The $\delta^{13}C_{org}$ curve includes expanded and well-defined trends where the carbon isotope segments C2 (upper part), C3, C4, C5, C6 and C7 (partial) of Menegatti et al.

(1998) can be identified (Fig. 2). These segments correlate with other sections (Fig. 6), and allow for the recognition of the early Aptian OAE 1a (~120 Ma) within the middle member of the Carbonero Formation. This is consistent with the sedimentological and biostratigraphic data provided by calcareous nannofossil assemblages (see section 2.2).

The interval between 2–28 m, including the complete lower member of the Carbonero Formation plus the lowermost part of its middle member, is assigned to the C2 segment. C-isotope segment C3 in Carbonero is clearly defined by a pronounced negative shift of ~2‰, across 19 metres (28–47 m), similar way to the $\delta^{13}C$ profile widely identified in the literature (e.g., Menegatti et al., 1998; Erba et al., 1999, 2010; de Gea et al., 2003; Millán et al., 2009; Kuhnt et al., 2011; Bottini and Mutterlose, 2012; Aguado et al., 2014a, b; Bottini et al., 2012, 2015). At Carbonero, the stratigraphic range of segment C3 of 19 m (Fig. 2) is more than 38 times thicker than in the Cismon Core in Southern Alps (Erba et al., 1999), about 7 m thicker than in the Cau section in the Prebetic of SE Spain (de Gea et al., 2003; Moreno-Bedmar et al., 2012; Naafs et al., 2016), and comparable to the thickness of the expanded section of La Bédoule in SE France (Kuhnt et al., 2011; Lorenzen et al., 2013; Moullade et al., 2015). This expanded thickness, joined to a high-density sampling, provides an unprecedented high-resolution record within the C3 segment, where the 'double trough' structure, first documented by Van Breugel et al (2007) and evidenced by Lorenzen et al. (2013) is easily identifiable (Fig. 6). As a result, new fluctuations and trends are apparent within the C3 segment of the Carbonero section, showing three distinctive negative peaks at 31.5 m, 39.5 m and 47 m, that allow its subdivision into seven subsegments (named 'a' to 'g' in Fig. 2).

A rapid positive excursion in the $\delta^{13}C$ of ~4‰–5‰ characterizes the C4 segment globally (Menegatti et al., 1998; Kuhnt et al., 2011; Lorenzen et al., 2013; Aguado et al., 2014a, b) (Fig. 2, 7). Similarly, the positive excursion associated with segment C4 in the $\delta^{13}C_{org}$ curve at Carbonero has an amplitude of ~4‰ with a thickness of about 5.5 m (47 m–52.5 m; Fig. 2). The subsequent stable but, slightly fluctuating and decreasing $\delta^{13}C_{org}$ trend (-25 to -26‰) is assigned to segment C5 and has a thickness of ~4.5 m (Fig. 2). A subsequent positive spike $\delta^{13}C_{org}$ spike of ~4.5‰ is assigned to segment C6 which extends from 60 m to 68.3 m. Finally, the fluctuating and overall decreasing trend from 68.3 m up to the end of the studied section at 80 m (and probably also extending into the overlying succession not covered in this study) is assigned to segment C7.

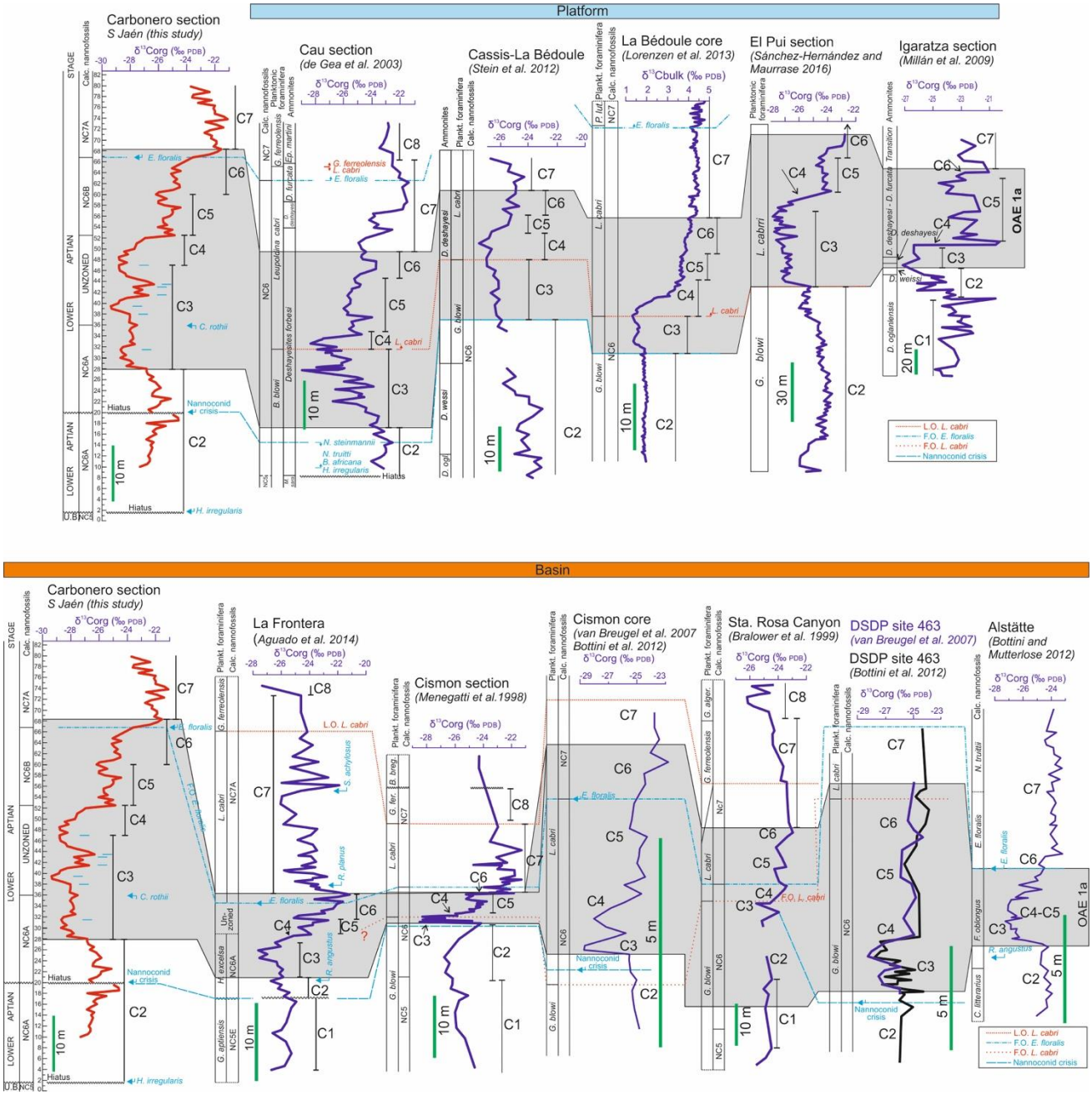

FIGURE 6. Correlation of the Carbonero section with selected sections from platform and basinal settings based on $\delta^{13}C$ stratigraphy. Biostratigraphic key events shown: L.O. *L. cabri* (=last occurrence of *Leupoldina cabri*), F.O. *E. floralis* (= first occurrence of *Eprolithus floralis*), F.O. *L. cabri* (= first occurrence of *Leupoldina cabri*) and the onset of the nannoconid crisis.

386 The correlation of the $\delta^{13}C_{org}$ profile of the Carbonero section with other published records of $\delta^{13}C_{org}$ and $\delta^{13}C_{carb}$
387 from different basins of pelagic and platform settings are shown in Fig. 6. Sections from pelagic settings are La Frontera,
388 from the Subbetic basin few kilometres away from the Carbonero section (Aguado et al., 2014a, b), Cismon, from the
389 southern Alps, where the C1 to C8 C-isotope segments where defined (Menegatti et al., 1998; Van Breuguel et al., 2007;
390 Bottini et al., 2012), Santa Rosa Canyon in Mexico (Bralower et al., 1999) and Alstätte in NW Germany (Bottini and
391 Mutterlose, 2012). The platform sections are the Cau section in SE Spain (de Gea et al., 2003; Naafs et al., 2016), the Cassis-
392 La Bédoule section (Stein et al., 2012) and La Bédoule core ($\delta^{13}C_{carb}$) in southern France (Lorenzen et al., 2013), the El Pui
393 section in the Pyrenees (Sánchez-Hernández and Maurrasse, 2016) and the Igaratza section in the Basque Basin in North-
394 Spain (Millan et al., 2009). The degree of correlation of the various $\delta^{13}C_{org}$ profiles is high among the different sections. The
395 main differences are related to the thickness of the C3 segment, which is generally thinner in distal pelagic sections, such
396 as the reference Cismon section and Santa Rosa Canyon, and thicker in platform and continental margin sections such as
397 La Bédoule, Cau, and Carbonero. This variation in thickness is mainly controlled by the subsidence rate but could also reflect
398 high sediment fluxes at marginal sites. Despite the differences in relative thicknesses, the original C-segments, trends, and
399 absolute values of $\delta^{13}C_{org}$ are in close agreement between Carbonero, the reference Cismon section and most of the other
400 OAE 1a sections. Importantly, the shape of segment C3 in the Carbonero section, with three negative peaks, is similar to
401 that observed in other expanded sections of the OAE 1a (Cau, Cassis-La Bédoule, El Pui; Fig. 6), and also to the Cismon core
402 where two negative excursions are identified (Van Breuguel et al., 2007; Bottini et al., 2012; Fig.6). Additionally, there are
403 also similar patterns in the TOC profiles with that observed at Cismon, with highest values in C4 after a first macimum at
404 the onset of C3 (Van Breuguel et al., 2007; Bottini et al., 2012). This correlation suggests that the $\delta^{13}C_{org}$ profile of the
405 Carbonero section might reflect a global signal and documents fluctuations in the global carbon cycle. The well-defined
406 carbon isotope curve of the Carbonero section provides a robust and highly detailed chemostratigraphic tool for temporal
407 correlation through the lower Aptian, even in the absence of paleontological data in some intervals. It also provides further
408 evidence for complex and episodic input of light carbon release events throughout the C3 interval.
409
410 *5.2. Sedimentation rates*
411 OAE 1a, defined as the interval C3–C6, has an estimated duration of ~1 to 1.3 Myr (Li et al., 2008; Malinverno et al., 2010;
412 Giraud et al., 2018). The thickness of this interval in Carbonero is 40 m, which gives an average sedimentation rate of 3–4
413 cm/kyr. This sedimentation rate is almost eight times higher than at the Cismon section (0.5 cm/kyr, Li et al., 2008), and it
414 is similar to, although slightly higher, that proposed for the La Bédoule section with values of 2.5–3.2 cm/kyr (Kuhnt et al.,

2011; Lorenzen et al., 2013). Although there is a general agreement about the duration of OAE 1a, estimates for the negative excursion (C3 segment) vary from 27–44 kyr (Li et al., 2008) to 22–47 kyr (Malinverno et al., 2010), from the reference Cismon section in the Italian Alps, to >100 kyr from La Bédoule in Southern France (Kuhnt et al., 2011; Lorenzen et al., 2013) and > 300 kyr from sections in central Turkey and the southern Alps (Hu et al., 2012; Huck et al., 2011). These differences are mostly related to the thickness of the C3 segment, which seems to be affected by high condensation in the Cismon section (see Kuhnt et al., 2011; Huck et al., 2011; Hu et al., 2012) potentially related to an acidification event (Erba et al., 2010), but can also be related to other processes. Nevertheless, more recent estimations from the Cismon core suggest a duration of C3 between 100 to 150 kyrs (Bottini et al., 2015). Following the estimates of Malinverno et al (2010) from Cismon for C3 (22–47 kyr), the Carbonero C3 segment (19 m thick) would have a sedimentation rate of ~40–86 cm/kyr, whereas the longer durations from expanded sections would give a sedimentation rate of 5–20 cm/kyr. An extensional tectonic pulse occurred during the early Aptian in the SIP (Martín-Chivelet et al., 2002; Castro et al., 2008; Skelton et al., 2019), which can account for a high subsidence pulse coeval to the deposition of the C3 segment. Nevertheless, following recent estimations from relatively expanded sections (see also Yamamoto et al., 2013), we consider that a duration of >100 kyr, probably in the range of ~300 kyr (as proposed by Huck et al 2011), giving a subsidence rate of ~6 cm/kyr is more consistent with the sedimentary evolution of the Carbonero section (de Gea et al., 2008B). For the segments C4 to C7 there is more agreement about their duration in the literature (Li et al., 2008; Malinverno et al., 2010; Bottini et al., 2015), giving more moderate sedimentation rates in the Carbonero section for the segments C4 (~1.7 cm/kyr), C5 (~1.3 cm/kyr) and C6 (~2.4 cm/kyr), consistent with lower subsidence rates after the main extensional episode on the SIP. Thus, it appears that the C3 interval at Carbonero and other marginal settings was characterised by a dramatic increase in sedimentation rates, as is observed during other rapid warming events such as the PETM (Carmichael et al., 2018, and references therein).

5.3. Environmental changes during the early Aptian

5.3.1 Elemental geochemistry

Distributions and stratigraphic changes in the concentration of selected elements in sediments have been used as marine environmental proxies, specifically for conditions at the sediment/water interface (e.g., Calvert and Pedersen, 2007). Among these environmental conditions, the most commonly investigated are redox state of the ambient seawater, productivity and continental sources, both fluvial and aeolian (e.g., Martínez-Ruiz et al, 2015).

444 Enrichment in RSTE elements is considered to be a pervasive character of sediments deposited under low oxygen
445 conditions and have been used in the investigation of OAEs (Tribovillard et al, 2006; Brumsack, 2006; Calvert and Pedersen,
446 2007; Algeo and Rowe, 2012, Westermann et al., 2010, 2013 among others). Because of the behaviour of RSTE in the water
447 column and during early diagenesis, their sensitivity to redox conditions is rather element-specific, and it is generally
448 recommended that a suite of RSTE (here V, Ni, U, Cr) be used for reconstructing palaeoredox conditions rather than a
449 single element (e.g., Tribovillard et al., 2006; Westermann et al., 2013). In addition to single elements, specific ratios of
450 RSTE have been proposed and used to infer redox conditions (Kimura and Wanatabe, 1991; Jones and Maning, 1994).
451 Chromium, V, Ni, Cr, and U accumulate in marine sediments above their crustal abundances under suboxic conditions, that
452 is in the absence of both oxygen and sulphide (Calvert and Pedersen, 2007). The U/Th, Ni/Co and V/Cr ratios were proposed
453 by Jones and Manning (2004) as indices for the interpretation of bottom water palaeo-oxygen concentrations, which have
454 provided important information on palaeoredox conditions in a large number of studies (e.g., Gallego-Torres et al., 2010;
455 Martinez-Ruiz et al., 2015; Paschal et al., 2019). Jones and Manning (2004) established numerical boundaries between oxic,
456 dysoxic and anoxic conditions, which are represented in Figure 3. The boundary between oxic, suboxic and anoxic
457 conditions as recorded by those ratios varies with different studies (e.g., Hoffman et al., 2008; Algeo and Maynard, 2004),
458 but in general increasing ratios have been correlated with increased anoxia (e.g., Marynowski et al., 2012). V concentration
459 as a redox proxy has been also normalized by Sc (Fig.3), as proposed by Kimura and Wanatabe (1991).
460 The RSTE elements (V, U, Cr) and ratios (U/Th, Ni/Co, V/Cr and V/Sc) at Carbonero show generally parallel
461 distributions across the section (Fig. 5), with three levels of enrichment: at the lower part of the C3 segment, upper part
462 of C4 and C5-C6 transition. In addition to these three distinctive peaks, the evolution of the profiles is rather variable,
463 suggesting instability in redox conditions across the segments C3 to C6 that correspond to the OAE 1a interval. These rapid
464 changes in redox conditions during OAE 1a have been previously detected in other basins of the western Tethys (e.g.,
465 Westermann et al., 2013; Charbonnier et al., 2018), and suggest a general instability with the development of three distinct
466 periods of dysoxia.
467 Marine productivity has been estimated on the basis of geochemical proxies such as total organic carbon (TOC),
468 organic phosphorus (P_{org}), and biogenic barium (Ba_{bio}) (e.g., Tribovillard et al., 2006; Calvert and Pedersen, 2007; Schoepfer
469 et al., 2015). The utility of TOC, P and Ba as palaeomarine productivity proxies depends on a dominantly marine source of
470 organic matter and favourable conditions for preservation in the sediment (Schoepfer et al., 2015). Palaeoproductivity
471 assessments should generally be made on the basis of multiple proxies (e.g., Schoepfer et al., 2015). Organic carbon,
472 representing the single largest constituent of organic matter, provides a direct proxy for productivity (e.g., Pedersen and

Calvert, 1990; Schoepfer et al., 2015). Although the concentration of TOC in sediments is also a function of the particle exportation ratio from shallow waters, the preservation of organic matter in the water column and in the sediment, and the dilution of organic carbon by lithogenic or biogenic components in the sediment (e.g., Tyson, 2001; Tribovillard et al., 2006; Calvert and Pedersen, 2007; Schoepfer et al., 2015; Paschal et al., 2019), TOC enrichment is widely used as a primary indicator of marine productivity. Barium has been most widely used as productivity proxy (e.g., Calvert and Pedersen, 2007; Martínez-Ruiz et al., 2015; Schoepfer et al., 2015; Martínez-Ruiz et al., 2019), occurring as barite. The barite has been mainly associated with biogenous aggregates in surface and near-surface waters, especially siliceous debris (Bishop, 1988), although recent studies have demonstrated the link between bacterial activity and marine barite formation through Ba bioaccumulation on microbial biofilms (Martinez-Ruiz et al., 2019). Nevertheless, other minerals can contain Ba, notably lithogenous material derived from crustal rocks; to correct total Ba contents for the contribution from such sources the Ba concentration has been normalized to Al (Calvert and Pedersen, 2007). The behaviour of Ba in sedimentary environments is complex and its interpretation as productivity proxy has several caveats (e.g. ,Calvert and Pedersen, 2007; Martínez-Ruiz et al., 2015). Schoepfer et al (2015) demonstrated that there is a large negative effect in biogenic barium under conditions of high bulk accumulation rate (BAR), probably due to reduced uptake of barium at the sediment-water interface. Sedimentary barite might undergo diagenetic changes and should be used cautiously as Ba migration is possible under severe sulphate depletion due to microbial sulphate reduction in porewaters (Brumsack et al., 1992), giving rise to the development of barite fronts or nodules (Bréhéret and Brumsack, 2000; Turgeon and Brumsack, 2006). Nevertheless, the variability of sedimentary Ba has become one of the most widely used proxies for palaeoproductivity (Schoepfer et al., 2015). Phosphorus is a limiting macro-nutrient for algal growth, being a structural and functional component of all organisms (Redfield, 1958), and its accumulation in marine sediments has been used as a palaeoproductivity proxy (e.g., Pedersen and Calvert, 2007). Organic matter is the ultimate source of most P in marine sediments (Schoepfer et al., 2015), whereas detrital P generally comprises less than 20% of total P (Algeo and Ingall, 2007). Consequently, total P is commonly used as a proxy for organically derived phosphorous (Schoepfer et al., 2015). P is preferentially recycled back into the water column under reducing conditions but can be effectively retained within the sediment under oxic to suboxic conditions (Föllmi, 1996; Algeo and Ingall, 2007). As a result of complex interactions between productivity, redox conditions and burial efficiency, P cannot be assumed to have a linear relation with primary productivity (Tribovillard et al., 2006). Nevertheless, P is considered as one of the most robust and widely applicable productivity proxies, being consistently more enriched in productive upwelling zones than in stagnant depositional basins (Brumsack, 2006).

501 The profiles for TOC, Ba/Al and P/Al all three exhibit two peaks in all parameters (lower part of C3 and upper part of C4
502 segments). Ba/Al ratios are generally higher than an average shale (ASV) (Wedepohl, 1991; Brumsack, 2006), which would
503 indicate elevated productivity during OAE 1a, albeit with rapid variations. The presence of barite concretions in the
504 Carbonero section has been related to a diagenetic process of segregation (Molina and Hernández-Molina, 1993) These
505 concretions are present in two levels located within the lower part of the section (C2 segment), but the presence of
506 carbonate concretions within the C3 and C4 segments support the presence of a diagenetic remobilization affecting the
507 section. The positive correlation of Ba and P with TOC in the two lower distinctive peaks shown by most proxies suggest a
508 sedimentary signal in the distribution of Ba, whereas the three intervals of high values recorded only in the Ba/Al ratios
509 which are not correlated by TOC at C2, middle part of C5 and middle part of C6 segments are considered to reflect
510 diagenetic processes of remobilization (Turgeon and Brumsack, 2006). The calcareous nannofossil nutrient index
511 reconstructed for pelagic sections (Aguado et al., 2014a; Bottini et al., 2015; Bottini and Erba, 2018) provide an alternative
512 and independent proxy to evaluate productivity across OAE 1a. Positive peaks of the NI, suggesting high productivity, are
513 recorded at the lower part of C3 segment (Aguado et al., 2014a; Bottini et al., 2015; Bottini and Erba, 2018) and around
514 the C4 isotopic segment (Bottini et al., 2015; Bottini and Erba, 2018), which is in agreement with the indicated by the
515 geochemical productivity proxies in the Carbonero section.

516 The most common element ratios that have been used as proxies for terrigenous supplies are Ti/Al, Zr/Al, K/Al,
517 Mg/Al, Rb/Al, and Si/Al (e.g., Hild and Brumsack, 1998; Niebuhr, 2005; Calvert and Pedersen, 2007; Engelke et al., 2018).
518 The Ti/Al and Zr/Al ratios have been used as a terrestrial aeolian source and grain-size proxy because Ti and Zr concentrate
519 in soils; due to their higher specific gravity than quartz, they are transported with the fine and medium sand quartz in many
520 sediments (Calvert and Pedersen, 2007). We have not used Si/Al ratio because of the presence of radiolarites in the section,
521 which would led to a significant contribution from biogenous Si. K/Al, Rb/Al and Mg/Al have been considered as proxies for
522 fluvial sources (Martínez et al., 2015; Aguado et al., 2016). In the late Quaternary in the Mediterranean, humid periods
523 characterized by lower aeolian input exhibit decreasing Ti/Al and Zr/Al ratios and enhanced K/Al and Mg/Al ratios (e.g.,
524 Warning and Brumsack, 2000; Nijenhuis et al., 2001), suggesting a preferential fluvial source for K and Mg, and an aeolian
525 source for Ti/Al, and Zr/Al (Martínez et al., 2015). However, distinguishing between aeolian and fluvial sources of certain
526 element ratios is difficult because both sources can provide the same detrital minerals (Martínez-Ruiz et al., 2015).

527 To explore the continental inputs, three elements considered as proxies for fluvial sources (Rb/Al, Mg/Al, and K/Al)
528 and two as proxies for aeolian sources (Ti/Al and Zr/Al) have been analysed (Fig. 3). In general, these proxies show parallel
529 patterns, with high-frequency oscillations, and three main peaks at the base of C3, upper part of C4 and middle part of C6

segments (Fig. 3). No significant differences are detected between fluvial and aeolian proxies, therefore they are considered collectively as terrestrial proxies. The comparison between profiles of RSTE and productivity proxies reveals interesting relationships: the two lower levels of enrichment in RSTE and productivity proxies are coincident with the enrichment in continental inputs and an inferred increase in sedimentation rates, suggesting a relationship between continental nutrient inputs, productivity and anoxia.

Collectively, these data suggest a variable depositional environment during OAE 1a with changes in redox conditions, productivity and continental input. We find three main episodes of enrichment of selected elements. The two first episodes (lower part of C3 and upper part of C4 segment) are related to an increase in productivity, anoxia and continental inputs, suggesting that increased nutrient input from the continent led to an increase in marine productivity, which changed the sedimentary redox conditions. These increases in productivity are also suggested from the calcareous nannofossil-derived NI in pelagic sections (Bottini et al., 2015; Bottini and Erba, 2018). For the first of these events, associated with the lower part of C3, this appears to have been driven by the release of isotopically depleted carbon into the ocean-atmosphere reservoir. The third episode of anoxia/dysoxia (C5/C6 transition), has no evidences of fertilization, as all terrestrial proxies present low values, as well as Ba/Al and P/Al, with the exception of TOC. This decrease in fertilization from the C4 to C5 segments onwards has been also recorded in other sections worldwide (Aguado et al., 2014a; Bottini et al., 2015). In this interval, the data suggest that oxygen depletion led to enhanced preservation of organic matter without a significant increase in productivity, probably related to a restricted water circulation (e.g., Arthur and Sageman, 1994; Westermann et al., 2013). This interpretation is also consistent with low P/Al values, as P can be recycled under low oxygen conditions (Föllmi, 1996; Algeo and Ingall, 2007).

Enrichments in RSTE, productivity and terrigenous inorganic proxies have been documented in the record of the OAE 1a from different basins, in the Western Tethys (Turgeon and Brumsack, 2006; Stein et al., 2012; Westermann et al., 2013; Charbonnier et al., 2018), Pyrenees (Sánchez-Hernández and Maurrasse, 2016), North German basin (Hild and Brumsack, 1998), Gulf of Mexico (Nuñez-Useche et al., 2015) and Pacific (Erba et al., 2015). These data clearly indicate the development of global perturbations in the marine environmental conditions during OAE 1a, similar to that documented in this study. These perturbations have been also recorded from other OAEs (e.g., OAE2, Westermann et al., 2014), and the PETM (Dickson et al., 2014), indicating to be a relevant feature of hyperthermals.

5.3.2 Biomarkers

5.3.2.1 Maturity assessment

559 Maturity assessment is key to contextualising and interpreting biomarker records (e.g., Peters et al., 2005). The most
560 powerful tools for assessing low to moderate maturity (with respect to oil generation) are those based on the relative
561 distribution of sterane and hopane isomers, along with *n*-alkane distributions. The 22S/(22S+22R) homohopane ratio of
562 c.a. 0.55, the sterane C_{29} - 20S/(20S+20R) ratio of ~0.5 and the *n*-alkane CPI ratio of c.a. 1, all fairly constant across the
563 section, collectively indicate a thermal maturity of the section near the peak state of oil generation (Mackenzie et al., 1980;
564 Seifert and Moldowan, 1980; Waples and Machihara, 1991). This is equivalent to a vitrinite reflectance between 0.65 and
565 0.85, according to Peters et al (2005). Other ratios more sensitive at this maturity level are C_{29} steranes ($C_{29}\beta\beta/\beta\beta+\alpha\alpha$), and
566 C_{30} hopanes ($\beta\alpha/\beta\alpha + \alpha\beta$), which both show a consistent vertical evolution with a slightly high maturity coinciding with the
567 C3 to mid C6 segments interval, that broadly coincides with the OAE 1a interval (Fig. 3). This slight stratigraphic variation
568 in thermal maturity has been also noted across OAE 1a in the Southern Alps (Cismon section; Van Breugel et al., 2007),
569 where the differences are more marked. These authors related these changes to input of organic matter from weathered
570 material from ancient mature rocks, and similar processes could be occurring here, especially given the very high
571 sedimentation rates inferred for C3 as discussed above.
572
573 5.3.2.2 Sources and environment
574 Short-chain *n*-alkanes, as well as pristane and phytane are typically used as indicators for marine organic matter sources,
575 whereas long-chain *n*-alkanes primarily reflect terrigenous sources (Eglinton and Hamilton, 1967). Thermal maturity affects
576 *n*-alkane distributions, mostly the odd to even distributions, which are c.a. 1 in the studied samples, but also reduces the
577 amount of high molecular weight (long-chain) relative to low molecular weight (short-chain) compounds. Given that OM
578 is thermally mature, low HMW/LMW ratios can be explained by the thermal maturity. Nevertheless, the presence of C_{25}-
579 C_{35} *n*-alkanes in several samples could reflect a terrigenous contribution, which is expected in this depositional setting. If
580 so, the vertical variations in the HMW/LMW ratio could reflect changes in the relative contribution of terrestrial *versus*
581 marine sources. Lowest values indicating highest marine contribution are recorded in the lower part of C3 and upper part
582 of C4 segment. Highest values occur within the C2 and C7 segments, where they are probably biased by a slight decrease
583 in thermal maturity (Fig. 4). Collectively, these data indicate that extracted organic matter derives from mixed terrigenous
584 and marine sources.
585 Steranes are the saturated hydrocarbon derivatives of sterols found in the cell membrane of eukaryotes, particularly
586 marine phytoplankton, and can therefore provide information regarding algal sources (Volkman et al., 1998; Peters, et al.,
587 2005). On the other hand, hopanes are produced by a range of bacteria (Ourisson et al., 1982). The relative contribution

588 of bacterial with respect to algal biomass is usually assessed using the ratio of total hopanes to total steranes [C_{27-30}
589 steranes/(C_{27-30} steranes + C_{27-35} hopanes)] (Moldowan et al., 1985). The hopane/sterane ratio (Fig. 4) exhibits a general
590 increase across the segments C3 to C5, punctuated with abrupt changes. This suggests a long-term but irregular increase
591 in the contribution from bacterial with respect to algal sources during the early parts of OAE 1a. In addition, terrigenous
592 organic matter can deliver hopanes derived from soil bacteria, also increasing the hopane/sterane ratio (e.g., Moldowan
593 et al., 1985).

594 The homohopane index (HHI: C_{35}/C_{31-35} hopanes) is a proxy for changes in redox conditions at the sediment-water
595 interface (Bishop and Farrimond 1995; Peters et al., 2005). In anoxic environments (HHI > 10%), the extended C_{35} side chain
596 is preserved due to sulfurization reactions, whereas shorter side-chain hopanes tend to be more abundant in oxic
597 environments as a result of side chain cleavage during oxidative reactions (Peters and Moldowan 1991; Sinninghé Damsté
598 et al., 1995). The HHI ranges from 1 to 10% (average 6.4% ± 2.5), with two peaks indicating enhanced dysoxia or anoxia in
599 the lower part of C3 segment, and from the uppermost part of C3 to C6, with maxima at the end of C4 and at the C4/C5
600 transition (Fig. 4). Other compounds indicative of anoxia in the water column (e.g., gammacerane and isorenieratane),
601 were not identified, suggesting that the extent of anoxia/dysoxia in the Carbonero basin was relatively limited.

602 The 2α-methylhopane index (2-MHI) has been used as an indicator of cyanobacterial inputs (Summons et al., 1999),
603 although additional sources have subsequently been reported (Rashby et al., 2007; Welander et al., 2010). Different
604 investigations have pointed out the high concentration of 2-methylhopanoids in sediments deposited during OAEs (Kuypers
605 et al., 2004b; Van Breugel et al., 2007; Blumemberg et al., 2013), as well as during other episodes of environmental change
606 (e.g., Paleocene-Eocene Thermal Maximum, Arreguín et al., 2014). Here, the 2-MHI index shows three main intervals of
607 enrichment, two within the C3 and another at the end of C4 to C5 segments, and other two less pronounced episodes in
608 C6 and C7 segments (Fig 3). Recent research suggests that presence of these compounds might indicate
609 paleoenvironmental stressing conditions, such as hypoxia, changes in pH or nitrogen fixation (Newman et al., 2016; Ricci
610 et al., 2016; Garby et al., 2017). Regardless, our results, alongside similar observations at Shatsky Rise (Dumitrescu and
611 Brassel, 2005) and Cismon (Van Breugel et al., 2007), suggest a similar ecological response to OAE 1a environmental change
612 as that observed for OAE 2, providing additional evidence for mechanistic similarities between these events. However, the
613 Carbonero record, with multiple peaks in 2-MHI suggest a complex series of environmental-ecological interactions.
614 Although these compounds cannot be used as taxonomic biomarkers for any particular group, they may be diagnostic for
615 the confluence of particular environmental parameters such as suboxia or anoxia, high osmolarity and limited fixed
616 nitrogen, collectively indicating ecological stress (Ricci et al., 2016).

617

618 5.3.3 Implications for palaeoenvironmental changes during OAE 1a

619 In order to assess the environmental changes recorded in the studied section and their relation to the perturbations in the
620 global carbon cycle, the evolution of the C-isotope record is compared to the organic and inorganic geochemical records
621 from Carbonero and with published data from different basins worldwide.

622 The earliest Aptian (C2 isotope segment) exhibits stable values in all parameters analysed, including low
623 concentrations of TOC and RSTE elements, corresponding to low productivity and generally arid environments (Aguado et
624 al 2014a) in a global context of a relatively stable carbon cycle. A regional small discontinuity is recorded in this interval,
625 and the resumption of sedimentation coincides with the onset of the "nannoconid crisis" and a subtle increase in TOC.
626 Calcareous nannofossil assemblages from a nearby section (La Frontera section, Aguado et al., 2014a), record a change to
627 broadly meso-eutrophic surface water conditions and warm climate with intermittent freshening, which was interpreted
628 as a shift towards more humid conditions around this time. This shift can account for a punctual increase in terrestrial
629 inputs recorded in trace elements and biomarkers (HMW/LMW), without a corresponding increase in the productivity
630 proxies. Similar patterns, with a short phase of increased fertility during the C2 segment have been observed in other
631 sections from the tehyan and pacific domains (Bottini et al., 2015)

632 The main change recorded in the Carbonero section corresponds to the negative excursion in $\delta^{13}C_{org}$ defining the
633 C3 segment (28-47 m) which shows a complex structure and three negative CIEs. The C3 segment is considered one of the
634 most striking features of OAE 1a and interpreted as the result of an input of light carbon into the ocean/atmosphere system
635 (e.g., Jenkyns, 2010). This carbon is generally thought to come from volcanisms and/or methane hydrate dissociation. One
636 potential way to distinguish between these two mechanisms is the timing, as methane hydrate with lower $\delta^{13}C$ values can
637 cause a rapid negative excursion through a short-lived release, whereas volcanic CO_2 emissions, with higher $\delta^{13}C$ values
638 could result in C-isotope negative excursions during gradual and long-lasting episodes (e.g., Mehay et al., 2009; Lorenzen
639 et al., 2013; Naafs et al., 2016). Based on sedimentation rate estimates from expanded sections, including the Carbonero
640 section, the complete negative excursion could have taken more than 100 kyrs. Such a long time span is predominantly
641 consistent with a volcanic CO_2 releasing episode (Naafs et al., 2016), although three abrupt negative CIEs within the C3
642 segment depicted in Carbonero (and other sections) could be related to short pulses of methane release superimposed on
643 a gradual (Jahren et al., 2005; Renard et al., 2005; Mehay et al., 2009; Naafs et al., 2016) or polyphasic (Bottini et al., 2012)
644 volcanic release. The timing of these negative CIEs could be astronomical as has been demonstrated for OAE 2 (Kuypers et

al., 2004a; Dickson et al., 2017), although a further analysis of cyclicity in the studied section is needed in order to confirm this hypothesis.

The lower part of segment C3 records the first episode of environmental perturbation in the Carbonero section, with RSTE enrichments and increased sedimentation rates coeval with a general perturbation in the biomarker distributions, indicating the development of anoxia/dysoxia near the sediment-water interface, along with an increase in productivity and continental inputs (e.g., Ti/Al) (Fig. 7). Collectively, all of the data point to an increase in fertilization and productivity leading to anoxia/dysoxia and a marked increase of bacterial over algal sources in the organic matter (hopane/sterane index). This is consistent with an intensification of the greenhouse conditions, which may have accelerated the hydrological cycle resulting in increased continental weathering and enhanced nutrient input from the continents to the ocean (Weissert, 1990; Föllmi, 2012; Westermann et al., 2013), which is commonly invoked as a critical aspect of OAE initiation (e.g., Bralower et al., 1999; Erba and Tremolada, 2004; Jenkyns, 2010; Monteiro et al., 2012; Westermann et al., 2013; Aguado et al., 2014a; Bottini et al., 2015). Additional mechanisms have been suggested to contribute to a further fertilization of the ocean, as the relative high sea-level during the early Aptian, which may have favored the reworking of sediments and soils by flooding of land areas (Jarvis et al., 2002; Westermann et al., 2013). The upper part of the C3 segment shows minor punctual increases in terrestrial markers and productivity, under generally well oxygenated waters. In general, the C3 interval is considered to be chararterised by increasing pCO_2 concentrations (e.g., Heimhofer et al 2004; Erba and Tremolada 2004; Erba et al., 2010, 2015; Naafs et al 2016) and temperatures (e.g., Kuhnt et al 2011; Bottini et al., 2015; Naafs and Pancost, 2016). Nevertheless, a short episode of cooling has been proposed during the lower part of C3 segment (Jenkyns 2018), that could be related to a CO_2 drawdown from OM deposition (Bottini et al., 2015; Bottini and Erba, 2018), or to a reduction in the CO_2 volcanic emissions (Bottini et al., 2015).

Collectively, the C3 segment records an episode of severe environmental change, with a general gradual increase in pCO_2 probably punctuated by pulses of accelerated rises leading to the spiky shape of the $\delta^{13}C$ profile recording a marked instability. These changes in pCO_2 and temperatures would have resulted in an intensification of the hydrological cycle, and subsequent increased input of nutrient into the ocean (e.g., Erba, 2004; Föllmi, 2012; Mutterlose and Bottini, 2013; Weissert and Erba 2004; Erba et al., 2015). The high productivity, indicated by the geochemistry but also by the presence of radiolarites within C3 segment, was probably the main factor controlling the oxygen depletion in the bottom waters. In this context, rapid changes in the environmental conditions affected the biomass, giving rise to a dominance of bacteria over algae (Kuypers et al., 2004b).

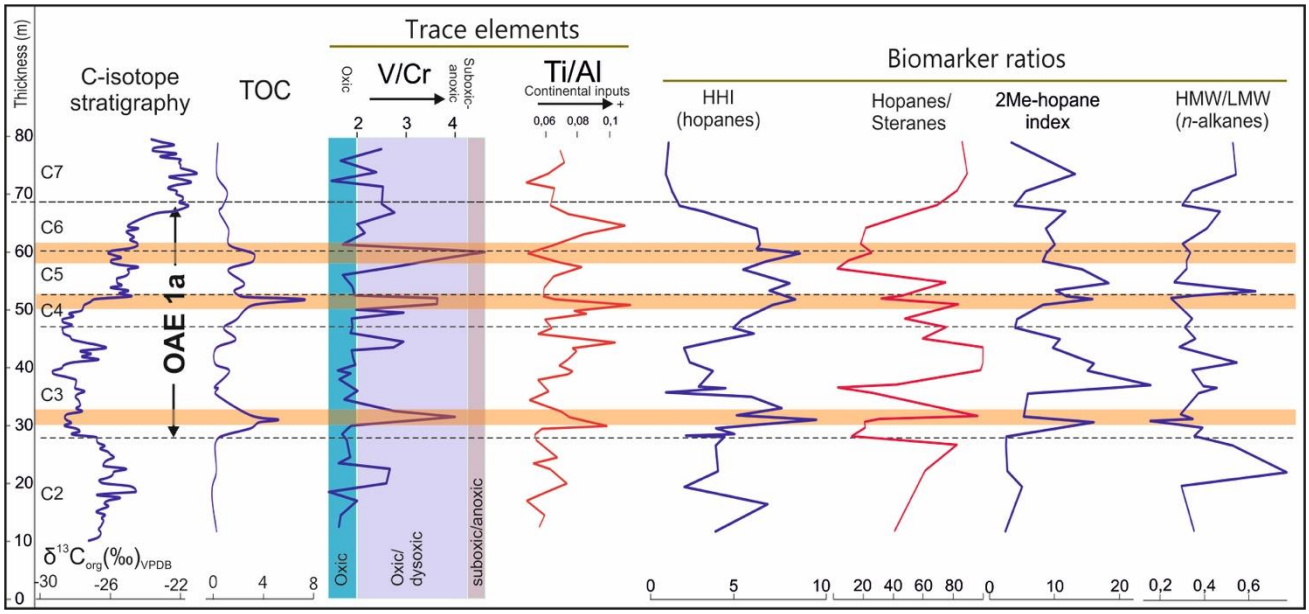

FIGURE 7. Selected elemental and biomarker ratios against C-isotope stratigraphy.

During the positive C-isotope excursion (segment C4), RSTEs and biomarkers exhibit an increase in anoxic conditions in the sediment-water interface, coincident with enhanced productivity, and increased terrestrial input, (as indicated by most of the elemental proxies). Estimated palaeotemperatures suggest a short episode of cooling (Dumitrescu et al., 2006; Kuhnt et al., 2011; Jenkyns, 2018), due to the decrease in CO_2 concentrations (Heimhofer et al., 2004; Naafs et al., 2016) associated with either enhanced burial of organic matter or a reduction in the inputs of CO_2 coupled with an increase in silicate weathering linked to an enhanced hydrological cycle (e.g., Lechler et al., 2015; Jenkyns, 2018). A possible oxygenation episode during this interval of cooling (Jenkyns, 2018) could correspond to that of the end of C4 segment recorded in Carbonero (Fig. 4), although further higher-resolution data for correlation are needed to elucidate the temporal relationships between these environmental changes.

The positive C-isotope trend was followed by an interval of stable values in $\delta^{13}C$ (C5 segment), characterized by a general recovery to pre-C3 values in most organic and inorganic indices. The exceptions are the 2Me-hopane and the hopane/sterane indexes, which are elevated in this interval indicating an ongoing ecological perturbation, perhaps related to environmental stress (Neuman et al., 2016; Ricci et al., 2016). This interval is followed by a third episode of increase in anoxia/dysoxia during the C5-C6 transition, indicated by enrichment in RSTE and biomarker HHI ratios, but with an interesting difference to the previous two episodes: in this episode there is no evidence for enhanced productivity nor terrestrial input (Fig. 7). These results point to a development of anoxia not linked to enhanced production in surface waters, but instead to possible deoxygenation of the marine bottom waters in the Subbetic basin. This interval is

693 characterized by a further increase in global temperatures (Dumitrescu et al., 2006; Bottini et al., 2015; Naafs and Pancost,
694 2016; Jenkyns, 2018), related to an increase in pCO_2 concentrations (Naafs et al., 2016), probably linked to a sustained
695 input of volcanic CO_2 (e.g., Tejada et al., 2009; Bottini et al., 2012). This evolution of the anoxia/dysoxia during the OAE 1a,
696 from an initial phase controlled by enhanced productivity followed by increased preservation due to the development of
697 anoxia during the OAE 1a can be explained by a model in which fertilization can account for oxygen depletion at a local
698 (basinal) scale (C3 interval), whereas the global consumption of oxygen due to widespread global organic matter
699 deposition, as indicated by the positive excursion in $\delta^{13}C$ values (C4–C5) would lead to an oxygen depletion in oceanic
700 bottom waters, when a critical threshold is passed as the production of organic matter exceeds the rate in which it is
701 oxidized (Robinson et al., 2004). This evolution from enhanced productivity to enhanced preservation during OAE 1a has
702 been also observed in different sections from the western Tethys (Westermann et al., 2013).

703 During the upper part of C6 and C7 segments, $\delta^{13}C_{org}$ values increase (C6) and reach the highest values before they
704 start to decrease (upper part of segment C7). Terrestrial inputs increase during C6, although redox and productivity indices
705 indicate a gradual return towards conditions of well oxygenated waters from the beginning of the C6 segment upwards.
706 Therefore, the highest $\delta^{13}C$ values are interpreted as the result of enhanced global light carbon burial, although no dysoxic
707 conditions affected the Subbetic Basin, as has been documented from sections worldwide, where the end of the
708 generalized anoxia coincides with the base of C7 segment (e.g., Bottini et al., 2015).

709 Ultimately, as both volcanic inputs and organic burial started to return to pre-OAE conditions, so do oxygenation
710 levels. Intriguingly, however, ecological changes, especially with respect to unicellular organisms (bacteria and algae),
711 persist. Elevated hopane/sterane ratios document a marked increase in bacterial sources over plants and algae, and a
712 further two peaks in 2-Me-hopanes (Fig. 7) collectively indicate an ongoing dominance of OAE-associated microbial
713 assemblages. Thus, the biomass did not completely recover to pre-OAE conditions during the C7 segment, despite the fact
714 that environmental conditions did. A persistent biotic (especially microbial) perturbation has been observed for other
715 events, e.g., the Permo-Triassic Boundary (Xie et al., 2004) and could indicate that recovery of biota would take a longer
716 period, due to persistence of perturbed ecological conditions favoring the microbial growth in the Subbetic basin, probably
717 in relation to a disruption in nutrients cycling (Newman et al., 2016; Ricci et al., 2016; Garby et al., 2017) or grazing pressure
718 (Xie et al., 2004) linked to the effects of the nannoconid crisis, or a combination of both.

719 The general evolution from an initial phase of enhanced productivity followed by increasing preservation, mirrored
720 by climate changes with cooling episodes punctuating the high temperature conditions has been also recorded in other
721 sections worldwide (e.g. Westermann et al., 2014; Bottini et al., 2015; Jenkyns, 2018), collectively indicating a complex

global perturbation of the climate and environmental conditions across the OAE 1a. The development of several episodes of potential drawdown of atmospheric CO_2 or reduction in volcanic input of this greenhouse gas leading to episodes of cooling seems to be coeval in different sections worldwide (Jenkyns, 2018), and broadly correlate to the three episodes of maximum anoxia and productivity recorded in the Carbonero section.

6. Conclusions

The Carbonero section from the Lower Aptian of the Subbetic basin provides an expanded and continuous stratigraphic record of OAE 1a. The $\delta^{13}C_{org}$ stratigraphy records the global C-isotope signal, with identification of previously defined segments. Local subsidence during deposition of segment C3 is considered to be the main cause of differences between sections. Nonetheless, correlation of the C-isotope profile with other sections revealed clear similarities with expanded sections deposited on highly subsiding areas, mostly during the lower part of the OAE 1a, and general agreement during the upper part. In particular, these reveal a far more complex negative carbon isotope excursion, associated with either episodic CO_2 inputs or a complex interplay between carbon inputs to the atmosphere-hydrosphere systems, productivity and preservation of organic matter.

Integration of organic and inorganic geochemistry has revealed generally well oxygenated conditions, punctuated by three episodes of anoxia/dysoxia in the water-sediment interface, under a general context of instability in the environmental conditions during the studied interval. The two first episodes of anoxia/dysoxia correlate with enhanced organic productivity during the main negative C-isotope excursion that represents the onset of the OAE 1a. They are placed at the final part of C-isotope negative excursions, probably occurred in response to CO_2 release, increased temperatures and associated hydrological change and weathering, resulting in fertilization-driven oxygen consumption and depletion. This was followed by the widely observed positive carbon isotope excursion, likely due to the burial of OM outpacing volcanic carbon inputs. Interestingly, the third episode of anoxia-dysoxia, which occurred later during the mayor positive C-isotope excursion, is not associated with fertilization, and perhaps instead reflects a general progressive depletion of oxygen during OAE 1a, linked to stagnation of marine waters.

The biomarkers distributions have revealed that, although most environmental proxies show a return to pre-OAE conditions during C7 C-isotope segment, a perturbation in microbial ecology persisted, probably indicating a delayed biotic recovery to the perturbation, linked to environmental stress.

Acknowledgements

This work is a contribution of the research projects CGL2014-55274-P and CGL2014-52546-P of the Spanish Ministry of Science and Technology, and Research Group RNM-200 (Junta de Andalucía). BDAN and RDP were funded by the European Research Council under the European Union's Seventh Framework Programme (FP/2007-2013) / ERC Grant Agreement number 340923 (T-GRES, awarded to RDP). BDAN also received funding through a Royal Society Tata University Research Fellowship. SF thanks the financial support granted for his postdoctoral by Capes (BEX 9085/11-4). Authors wish to thank two anonymous reviewers who improved the manuscript by their useful suggestions.

References

Aguado, R., 1994. Nannofósiles del Cretácico de la Cordillera Bética. Bioestratigrafía, PhD Thesis, Universidad de Granada, Granada, 413 pp.

Aguado, R., de Gea, G.A., Castro, J.M., O'Dogherty, L., Quijano, M.L., Naafs, B.D.A., Pancost, R.D., 2014a. Late Barremian–early Aptian dark facies of the Subbetic (Betic Cordillera, southern Spain): Calcareous nannofossil quantitative analyses, chemostratigraphy and palaeoceanographic reconstructions. Palaeogeography, Palaeoclimatology, Palaeoecology 395, 198–221.

Aguado, R., de Gea, G.A., O'Dogherty, L., 2014b. Integrated biostratigraphy (calcareous nannofossils, planktonic foraminifera, and radiolaria) of an uppermost Barremian–lower Aptian pelagic succession in the Subbetic Basin (southern Spain). Cretaceus Research 51, 153–173.

Aguado, R., Molina, J.M., O'Dogherty, L., 1993. Bioestratigrafía y litoestratigrafía de la Formación Carbonero (Barremiense-Albiense?) en la transición Subbético Externo–Subbético Medio (Sur de Jaén). Cuadernos de Geología Ibérica 17, 325–344.

Aguado, R., O'Dogherty, L., Sandoval, J., 2008. Fertility changes in surface waters during the Aalenian (mid Jurassic) of the Western Tethys as revealed by calcareous nannofossils and carbon-cycle perturbations. Marine Micropaleontology 68, 268–285.

Aguado, R., Reolid, M., Molina, E., 2016. Response of calcareous nannoplankton to the Late Cretaceous Oceanic Anoxic Event 2 at Oued Bahloul (central Tunisia). Palaeogeography, Palaeoclimatology, Palaeoecology 459, 289–305.

779 Algeo, T.J., Ingall, E., 2007. Sedimentary Corg:P ratios, Paleocean ventilation, and Phanerozoic atmospheric pO2.
780 Palaeogeography, Palaeoclimatology, Palaeoecology 256, 130–155.

781 Algeo, T.J., Maynard, J.B., 2004. Trace-element behavior and redox facies in core shales of Upper Pennsylvanian Kansas-
782 type cyclothems. Chemical Geology 206, 289-318.

783 Algeo T. J., Rowe H., 2012. Paleoceanographic applications of trace-metal concentration data. Chemical Geology 324–325,
784 6–18.

785 Ando, A., Kaiho, K., Kawahata, H., Kakegawa, T., 2008. Timing and magnitude of Early Aptian extreme warming: unraveling
786 primary $\delta^{18}O$ variation in indurated pelagic carbonates at Deep Sea Drilling Project Site 463, central Pacific Ocean.
787 Palaeogeography, Palaeoclimatology, Palaeoecology 260, 463–476.

788 Ando, A., Kakegawa, T., Takashima, R., Saito, T., 2002. New perspective on Aptian carbon isotope stratigraphy: data from
789 $\delta^{13}C$ records of terrestrial organic matter. Geology 30, 227–230.

790 Arreguín-Rodríguez, G.J., Alegret, L., Sepúlveda, J., Newman, S. and Summons, R.E., 2014. Enhanced terrestrial input
791 supporting the *Glomospira* acme across the Paleocene-Eocene boundary in Southern Spain. Micropaleontology
792 60, 43–51.

793 Arthur M. A. and Sageman B. B., 1994. Marine black shales: depositional mechanisms and environments of ancient
794 deposits. Ann. Rev. Earth Planet. Sci. 22, 499–551.

795 Azéma, J., Foucault, A., Fourcade, E., García Hernández, M., González Donoso, J.M., Linares, A., Linares, D., López Garrido,
796 A.C., Rivas, P., Vera, J.A., 1979. Las microfacies del Jurásico y Cretácico de las Zonas Externas de las Cordilleras
797 Béticas. Universidad de Granada (83 pp.).

798 Beerling, D.J., Royer, D.L., 2002. Fossil plants as indicators of the Phanerozoic global carbón cycle. Annual Review of Earth
799 and Planetary Sciences 30, 527–556.

800 Bishop, J.K.B., 1988. The barite–opal-organic carbon association in oceanic particulate matter. Nature 332, 341–343.

801 Bishop, N., Farrimond, P., 1995. A new method of comparing extended hopane distributions. Organic Geochemistry 23,
802 987–990.

803 Blättler, C.L., Jenkyns, H.C., Reynard, L.M., Henderson, G.M., 2011. Significant increases in global weathering during
804 Oceanic Anoxic Events 1a and 2 indicated by calcium isotopes. *Earth and Planetary Science Letters* 309, 77-88.
805 https:/doi.org/ 10.1016/j.epsl.2011.06.029

Blumenberg, M., Berndmeyer, C., Moros, M., Muschalla, M., Schmale, O., Thiel, V., 2013. Bacteriohopanepolyols record stratification, nitrogen fixation and other biogeochemical perturbations in Holocene sediments of the central Baltic Sea. Biogeosciences 10, 2725–2735.

Bottini, C., Cohen, A.S., Erba, E., Jenkyns, H.C., Coe, A.L., 2012. Osmium isotope evidence for volcanism, weathering and ocean mixing during the early Aptian OAE 1a. Geology 40, 583–586. https:/doi.org/10.1130/G33140.1

Bottini, C., Erba, E., 2018. Mid-Cretaceous paleoenvironmental changes in the western Tethys. Climate of the Past 14, 1147–1163. https://doi.org/10.5194/cp-14-1147-2018

Bottini, C., Erba, E., Tiraboschi, D., Jenkyns, H.C., Schouten, S., Sinninghe Damsté, J.S., 2015. Climate variability and ocean fertility during the Aptian Stage. Climate of the Past 11 (3), 383-402. https:/doi.org/10.5194/cp-11-383-2015

Bottini, C., Mutterlose, J., 2012. Integrated stratigraphy of Early Aptian black shales in the Boreal Realm: calcareous nannofossil and stable isotope evidence for global and regional processes. Newsletters on Stratigraphy 45, 115–137.

Bralower, T.J., CoBabe, E., Clement, B., Sliter, W.V., Osburn, C.L., Longoria, J., 1999. The record of global change in Mid-Cretaceous (Barremian–Albian) sections from the Sierra Madre, northeastern Mexico. Journal of Foraminiferal Research 29, 418–437.

Bralower, T.J., Leckie, R.M., Sliter, W.V., Thierstein, H.R., 1995. An integrated Cretaceous microfossil biostratigraphy. The Society of Economic Paleontologists and Mineralogists Special Publication 54, 65–79.

Bray, E.E., Evans, E.D. 1961. Distribution of n-paraffins as a clue to recognition of source beds. Geochimica et Cosmochimica Acta, 22, 2-15. https:/doi.org/10.1016/0016-7037(61)90069-2

Bréhéret, J.G., Brumsack,H.J., 2000. Barite concretions as evidence of pauses in sedimentation in the Marnes Bleues Formation of the Vocontian Basin (SE France). Sedimentary Geology 130, 205–228.

Brumsack, H.J., 2006. The trace metal content of recent organic carbon-rich sediments: implications for Cretaceous black shale formation. Palaeogeography, Palaeoclimatology, Palaeoecology 232, 344–361.

Brumsack, H.J., Zuleger, E., Gohn, E., Murray, R.W., 1992. Stable and radiogenic isotopes in pore waters from Leg 127, Japan Sea. In: Pisciotto, K.A., Ingle Jr., J.C., von Breymann,M.T., Barron, J., et al. (Eds.), Proc. Ocean Drill. Project 127/128 Part 1, pp. 635–650.

832 Calvert, S.E., Pedersen, T.F., 2007. Chapter Fourteen-Elemental Proxies for Palaeoclimatic and Palaeoceanographic
833 Variability in Marine Sediments: Interpretation and Application. In: Developments in Marine Geology 1, pp. 567–
834 644.
835 Carmichael, M.J., Pancost, R.D., Lunt, D.J. 2018. Changes in the occurrence of extreme precipitation events at the
836 Paleocene–Eocene thermal maximum. Earth and Planetary Science Letters, 501, 24-36. https:/doi.org/
837 10.1016/j.epsl.2018.08.005
838 Castro, J.M., de Gea, G.A., Ruiz-Ortiz, P.A., Nieto, L.M., 2008. Development of carbonate platforms on an extensional (rifted)
839 margin. The Valanginian–Albian record of the Prebetic of Alicante (SE Spain). Cretaceous Research 29, 848–860.
840 Charbonnier, G., Adatte, T., Spangenberg, J.E., Föllmi, K.B., 2018. The expression of early Aptian to latest Cenomanian
841 oceanic anoxic events in the sedimentary record of the Briançonnais domain. Global and Planetary Change 170,
842 76–92.
843 Chumakov, N.M., Zharkov, M.A., Herman, A.B., Doludenko, M.P., Kalandadze, N.N., Lebedev, E.L., Ponomarenko, A.G.,
844 Rautian, A.S., 1995. Climatic belts of the mid-Cretaceous time. Stratigraphy and Geological Correlation 3, 241–
845 260.
846 de Gea, G.A., 2004. Bioestratigrafía y eventos del Cretácico Inferior en las Zonas Externas de la Cordillera Bética. PhD thesis,
847 Universidad de Jaén, Servicio de Publicaciones de la Universidad de Jaén, 658 pp.
848 de Gea, G.A., Aguado, R., Castro, J.M., 2008a. Variaciones en el registro isotópico del carbono en dos secciones de edad
849 Aptiense inferior en la zona de transición entre el Subbético Externo y el Subbético Medio (Cordilleras Béticas,
850 Provincia de Jaén). Geogaceta 44, 191–194.
851 de Gea, G.A., Aguado, R., Castro, J.M., Molina, J.M., O'Dogherty, L., Ruiz Ortiz, P.A., 2008b. Lower Aptian Subbetic organic-
852 rich facies, radiolarites and associated deposits: the local expression of Oceanic Anoxic Event 1a (Carbonero
853 Formation, southern Spain). Cretaceous Research 29, 861–870.
854 de Gea, G.A., Aguado, R., Castro, J.M., Molina, J.M., Ruiz Ortiz, P.A., 2008c. Registro del evento anóxico del Aptiense inferior
855 en la cuenca subbética (Sur de Jaén): La Formación Carbonero. Geotemas 10, 135–138.
856 de Gea, G.A., Castro, J.M., Aguado, R., Ruiz Ortiz, P.A., Company, M., 2003. Lower Aptian carbo*n*-isotope stratigraphy from
857 a distal carbonate shelf setting: the Cau section, Prebetic Zone, SE Spain. Palaeogeography, Palaeoclimatology,
858 Palaeoecology 200, 207–219.
859 Demaison, G.J., Moore, G.T., 1980. Anoxic environments and oil source bed genesis. Organic Geochemistry 2, 9–31.

860 Dickson, A. J., Rees-Owen, R., März, L.C., Coe, A.L., Cohen, A.S., Pancost, R.D., Taylor, K., Shcherbinina, E., 2014. The spread
861 of marine anoxia on the northern Tethys margin during the Paleocene-Eocene Thermal Maximum.
862 Paleoceanography 29, 471–488. https:/doi.org/10.1002/2014PA002629.

863 Dickson, A.J., Saker-Clark, M., Jenkyns, H.C., Bottini, C., Erba, E., Russo, F., Gorbanenko, O., Naafs, B.D.A., Pancost, R.D.,
864 Robinson, S.A., van den Boorn, S.H.J.M., Idiz, E., 2017. A Southern Hemisphere record of global trace-metal
865 drawdown and orbital modulation of organic-matter burial across the Cenomanian–Turonian boundary (Ocean
866 Drilling Program Site 1138, Kerguelen Plateau). Sedimentology, 64 (1), 186-203.
867 https:/doi.org/10.1111/sed.12303

868 Didyck, B.M., Simoneit, B.R.T., Brassel, S.C., Eglinton, G., 1978. Organic geochemical indicators of palaeoenvironmental
869 conditions of sedimentation. Nature 272, 216–222.

870 Dumitrescu, M., Brassell, S.C., 2005. Biogeochemical assessment of sources of organic matter and paleoproductivity during
871 the Early Aptian Oceanic Anoxic Event at Shatsky Rise, ODP Leg 198. Organic Geochemistry 36, 1002–1022.

872 Dumitrescu, M., Brassell, S.C., Schouten, S., Hopmans, E.C., Sinninghe-Damste, J.S., 2006. Instability in tropical Pacific sea-
873 surface temperatures during the early Aptian. Geology 34, 833–836.

874 Eglinton, G., Hamilton, R.J., 1967. Leaf epicuticular waxes. Science 156, 1322–1335.

875 Engelke, J., Linnert, C., Niebuhr, B., Schnetger, B., Brumsack, H.J., Mutterlose, J., Wilmsen, M., 2018. Tracking Late
876 Cretaceous environmental change: Geochemical environment of the upper Campanian to lower Maastrichtian
877 chalks at Kronsmoor, northern Germany. Cretaceous Research 84, 323-339. https:/doi.org/
878 0.1016/j.cretres.2017.10.00

879 Erba, E., 1994. Nannofossils and superplumes: The early Aptian 'nannoconid crisis. Paleoceanography 9, 483–501.
880 https:/doi.org/10.1029/94PA00258.

881 Erba, E., Bottini, C., Weissert, H.J., Keller, C.E., 2010. Calcareous nannoplankton response to surface-water acidification
882 around Oceanic Anoxic Event 1a. Science 329, 428–432.

883 Erba, E., Channell, J.E.T., Claps, M., Jones, C., Larson, R., Opdyke, B., Premoli Silva, I., Riva, A., Salvini, G., Torricelli, S., 1999.
884 Integrated stratigraphy of the Cismon APTICORE (Southern Alps, Italy): a "reference section" for the Barremian–
885 Aptian interval at low latitudes. Journal of Foraminiferal Research 29, 371–391.

886 Erba, E., Duncan, R.A., Bottini, C., Tiraboschi, D., Weissert, H., Jenkyns, H.C., Malinverno, A., 2015. Environmental
887 consequences of Ontong Java Plateau and Kerguelen Plateau volcanism. In: The Origin, Evolution, and

888 Environmental Impact of Oceanic Large Igneous Provinces (C.R. Neal, W.W. Sager, T. Sano, T., y E. Erba, eds.).
889 Geological Society of America Special Paper 511.
890 Erba, E., Tremolada, F., 2004. Nannofossil carbonate fluxes during the Early Cretaceous: phytoplankton response to
891 nutrification episodes, atmospheric CO_2, and anoxia. Paleoceanography 19. https:/doi.org/10.1029/2003PA00084
892 (PA1008).
893 Föllmi, K.B., 1996. The phosphorus cycle, phosphogenesis and marine phosphate-rich de- posits. Earth Science Reviews 40,
894 55–124.
895 Föllmi, K.B., 2012. Early Cretaceous life, climate and anoxia. Cretaceous Research 35, 230–257.
896 Föllmi, K.B., Godet, A., Bodin, S., Linder, P., 2006. Interactions between environmental change and shallow water carbonate
897 buildup along the northern Tethyan margin and their impact on the Early Cretaceous carbon isotope record.
898 Paleoceanography 21, PA4211 https://dx.doi.org/10.1029/2006PA001313.
899 Foster, G.L., Hull, P., Lunt, D.J., Zachos, J.C., 2018. Placing our current 'hyperthermal' in the context of rapid climate change
900 in our geological past. Royal Society of London Philosophical Transactions. A 376: 20170086.
901 https://dx.doi.org/10.1098/rsta.2017.0086
902 Gallego-Torres, D., Martínez-Ruiz, F., De Lange, G.J., Jimenez-Espejo, F.J., Ortega-Huertas, M., 2010. Trace-elemental
903 derived paleoceanographic and paleoclimatic conditions for Pleistocene Eastern Mediterranean sapropels.
904 Palaeogeography, Palaeoclimatology, Palaeoecology 293, 76-89.
905 Garby, T.J., Matys, E.D., Ongley, S.E., Salih, A., Larkum, A.W., Walter, M.R., Summons, R.E., Neilan, B.A., 2017. Lack of
906 methylated hopanoids renders the cyanobacterium *Nostoc punctiforme* sensitive to osmotic and pH stress.
907 Applied and Environmental Microbiology, 83 (13), https:/doi.org/10.1128/AEM.00777-17
908 García-Hernández, M., López Garrido, A.C., Sanz de Galdeano, C., Vera, J.A., Rivas, P., 1980. Mesozoic paleogeographic
909 evolution in the External Zones of the Betic Cordillera (Spain). Geologie en Mijnbouw 59, 155–168.
910 Giraud, F., Pittet, B., Grosheny, D., Baudin, F., Lécuyer, C., Sakamoto, T., 2018. The palaeoceanographic crisis of the Early
911 Aptian (OAE 1a) in the Vocontian Basin (SE France). Palaeogeography, Palaeoclimatology, Palaeoecology 511, 483-
912 505. https:/doi.org/10.1016/j.palaeo.2018.09.014
913 Gröcke, D.R., Hesselbo, S.P., Jenkyns, H.C., 1999. Carbon-isotope composition of Lower Cretaceous fossil wood: ocean–
914 atmosphere chemistry and relation to sea-level change. Geology 27, 155–158.

915 Hay, W., 2017. Toward understanding Cretaceous climate—An updated review. Science China Earth Sciences 60, 5-19.

916 Heimhofer, U., Hochuli, P.A., Herrle, J.O., Andersen, N., Weissert, H., 2004. Absence of major vegetation and
917 palaeoatmospheric pCO_2 changes associated with oceanic anoxic event 1a (Early Aptian, SE France). Earth and
918 Planetary Science Letters 223, 303–318.

919 Heldt, M., Mutterlose, J., Berner, U., and Erbacher, J., 2012. First high-resolution $\delta^{13}C$-records across black shales of the
920 Early Aptian Oceanic Anoxic Event 1a within the mid-latitudes of northwest Europe (Germany, Lower Saxony
921 Basin). Newsletters on Stratigraphy, 45, 151–169.

922 Hild, E., Brumsack, H.J., 1998. Major and minor element geochemistry of Lower Aptian sediments from the NW German
923 Basin (core Hoheneggelsen KB 40). Cretaceous Research 19, 615-633. DOI: 10.1006/cres.1998.0122

924 Hochuli, P.A., Menegatti, A.P., Weissert, H., Riva, A., Erba, E., Premoli Silva, I., 1999. Episodes of high productivity and
925 cooling in the early Aptian Alpine Tethys. Geology 27, 657–660.

926 Hoffman, D., Algeo, T.J., Maynard, B., Joachimski, M.M., Hower, J.C., Jaminski, J., 1998. Regional and stratigraphic variation
927 in bottomwater anoxia in offshore core shales of Upper Pennsylvanian cyclothems from the Eastern Midcontinent
928 Shelf (Kansas), USA. In: Schieber, J., Zimmerle, W., Sethi, P.S. (Eds.), Shales and Mudstones. 1. Schweizerbartische
929 Verlagsbuchhandlung, Stuttgart, Germany, pp. 243–269.

930 Hu, X., Zhao, K., Yilmaz, I.O., Li,, Y., 2012. Stratigraphic transition and palaeoenvironmental changes from the Aptian oceanic
931 anoxic event 1a (OAE1a) to the oceanic red bed 1 (ORB1) in the Yenicesihlar section, central Turkey. Cretaceous
932 Research 38, 40–51.

933 Huck, S., Heimhofer, U., Rameil, N., Bodin, S., Immenhauser, A., 2011. Strontium and carbon-isotope chronostratigraphy
934 of Barremian–Aptian shoal-water carbonates: Northern Tethyan platform drowning predates OAE 1a. Earth and
935 Planetary Science Letters 304, 547–558.

936 Jahren, A.H., Conrad, C.P., Crystal Arens, N., Mora, G., Lithgow-Bertelloni, C., 2005. A plate tectonic mechanism for
937 methane hydrate release along subduction zones. Earth and Planetary Science Letters 236, 691–704.

938 Jarvis, I., Lignum, J.S., Gröcke, D.R., Jenkyns, H.C., Pearce, M.A., 2011. Black shale deposition, atmospheric CO_2 drawdown,
939 and cooling during the Cenomanian–Turonian Oceanic Anoxic Event. Paleoceanography 26, PA3201.
940 https:/doi.org/10.1029/2010PA002081

941 Jarvis I., Mabrouk A., Moody R. T. J., de Cabrera S., 2002. Late Cretaceous (Campanian) carbon isotope events, sea-level
942 change and correlation of the Tethyan and Boreal realms. Palaeogeography, Palaeoclimatology, Palaeoecology
943 188, 215–248.
944 Jenkyns, H.C., 1995. Carbon isotope stratigraphy and paleoceanographic significance of the Lower Cretaceous shallow
945 water carbonates of Resolution Guyot, mid-Pacific Mountains. In: Winterer, E.L., Sager, W.W., Firth, V.J., Sinton,
946 M. (Eds.), Proceedings of the Ocean Drilling Program, Scientific Results, 143. College Station, Texas, pp. 89–97.
947 Jenkyns H. C., 1999. Mesozoic anoxic events and palaeoclimate. Zentrallblatt für Geologie und Paläontologie 1997, 943–
948 949.
949 Jenkyns, H.C., 2003, Evidence for rapid climate change in the Mesozoic–Palaeogene greenhouse world. Royal Society of
950 London Philosophical Transactions, A. 361, 1885–1916. https:/doi.org/10.1098/rsta.2003.1240
951 Jenkyns, H.C., 2010. Geochemistry of oceanic anoxic events. Geochemistry Geophysics Geosystem 11, Q03004.
952 https:/doi.org/10.1029/2009GC002788.
953 Jenkyns, H.C., 2018. Transient cooling episodes during Cretaceous Oceanic Anoxic Events with special reference to OAE 1a
954 (Early Aptian). Phil. Trans. R. Soc. A 376: 20170073. https://dx.doi.org/10.1098/rsta.2017.0073
955 Jones, B.A., Manning, D.A.C., 1994. Comparison of geochemical indices used for the interpretation of palaeoredox
956 conditions in ancient mudstones. Chemical Geology 111, 111–129.
957 Jones., C.E., Jenkyns, H.C., 2001. Seawater strontium isotopes, oceanic anoxic events, and seafloor hydrothermal activity
958 in the Jurassic and Cretaceous. American Journal of Science 301, 112–149. https:/doi.org/10.2475/ajs.301.2.112
959 Kidder, D.L., Worsley, T.R., 2010. Phanerozoic Large Igneous Provinces (LIPs), HEATT (Haline Euxinic Acidic Thermal
960 Transgression) episodes, and mass extinctions. Palaeogeography, Palaeoclimatology, Palaeoecology 295, 162-191.
961 https:/doi.org/10.1016/j.palaeo.2010.05.036
962 Kimura, H., Wanatabe, Y., 1991. Oceanic anoxia at the Precambrian-Cambrian boundary. Geology 29, 995-998.
963 Kuhnt, W., Holbourn, A., Moullade, M., 2011. Transient global cooling at the onset of early Aptian oceanic anoxic event
964 (OAE) 1a. Geology 39, 323–326.
965 Kump, L.R., Brantley, S.L., Arthur, M.A., 2000. Chemical weathering, atmospheric CO2, and climate. Annu. Rev. Earth Planet.
966 Sci. 28, 611–667. https:/doi.org/ 10.1146/annurev.earth.28.1.611

967 Kuypers, M.M., Lourens, L., Rijpstra, W.I.C., Pancost, R.D., Nijenhuis, I.A., Sinninghe-Damsté, J.S., 2004a. Orbital forcing of
968 organic carbon burial in the proto-North Atlantic during Oceanic Anoxic Event 2. Earth and Planetary Science
969 Letters 228, 465–482.
970 Kuypers, M.M., van Breugel, Y., Schouten, S., Erba, E., Sinninghe Damsté, J.S., 2004b. N_2-fixing cyanobacteria supplied
971 nutrient N for Cretaceous oceanic anoxic events. Geology 32, 853-856.
972 Larson, R.L., and Erba, E., 1999. Onset of the mid-Cretaceous greenhouse in the Barremian–Aptian: Igneous events and the
973 biological, sedimentary and geochemical responses. Paleoceanography 14, 663–678.
974 https:/doi.org/10.1029/1999PA900040
975 Lechler, M., Pogge von Strandmann, P.A.B, Jenkyns, H.C., Prossera, G. Parente, M., 2015. Lithium-isotope evidence for
976 enhanced silicate weathering during OAE1a (Early Aptian Selli event). Earth and Planetary Science Letters 432,
977 210–222.
978 Li, Y.X., Bralower, T.J., Montañez, I.P., Osleger, D.A., Arthur, M.A., Bice, D.M., Herbert, T.D., Erba, E., Premoli Silva, I., 2008.
979 Toward an orbital chronology for the early Aptian Oceanic Anoxic Event (OAE1a, 120 Ma). Earth and Planetary
980 Science Letters 271, 88–100.
981 Lorenzen, J., Kuhnt, W., Holbourn, A., Flögel, S., Moullade, M., Tronchetti, G., 2013. A new sediment core from the
982 Bedoulian (Lower Aptian) stratotype at Roquefort-La Bédoule, SE France. Cretaceous Research 39, 6-16.
983 Luciani, V., Cobianchi, M., Jenkyns, H.C., 2001. Biotic and geochemical response to anoxic events: the Aptian pelagic
984 succession of the Gargano Promontory (southern Italy). Geological Magazine 138, 277–298.
985 Mackenzie, A.S., Patience, R.L., Maxwell, J.R., Vandenbroucke, M., Durand, B., 1980. Molecular parameters of maturation
986 in the Toarcian shales, Paris Basin, France—I. Changes in the configurations of acyclic isoprenoid alkanes, steranes
987 and triterpanes. Geochimica et Cosmochimica Acta 44, 1709–1721.
988 Malinverno, A., Erba, E., Herbert, T.D., 2010. Orbital tuning as an inverse problem: chronology of the early Aptian oceanic
989 anoxic event 1a (Selli Level) in the Cismon APTICORE. Paleoceanography 25, PA2203.
990 https:/doi.org/10.1029/2009PA001769
991 Martín-Chivelet, J., Berasategui, X., Rosales, I., Vilas, L., Vera, J.A., Caus, E., Gráfe, K.U., Mas, R., Puig, C., Segura, M., Robles,
992 S., Floquet, M., Quesada, S., Ruiz-Ortiz, P.A., Frenegal-Martínez, M.A., Salas, R., García, A., Martín-Algarra, A., Arias,
993 C., Meléndez, M., Chacón, B., Molina, J.M., Sanz, J.L., Castro, J.M., García-Hernández, M., Carenas, B., García-

Hidalgo, J., Gil J., Ortega, F., 2002. Cretaceous, in: Gibbons, W. and Moreno, T. (Eds.), The Geology of Spain. The Geological Society, London, pp. 255–292.

Martinez-Ruiz, F, Kastner, M., Gallego-Torres, D., Rodrigo-Gámiz, M., Niero-Moreno, V., Ortega-Huertas, M., 2015. Paleoclimate and paleoceanography over the past 20,000 yr in the Mediterranean Sea Basins as indicated by sediment elemental proxies. Quaternary Science Reviews 107, 25–46.

Martínez-Ruiz, F., Paytan, A., Gonzalez-Muñoz, M.T., Jroundi, F., Abad, M.M., Lam, P.J., Bishop, J.K.B., Horner, T.J., Morton, P.L., Kastner, M., 2019. Barite formation in the ocean: Origin of amorphous and crystalline precipitates. Chemical Geology 511, 441-451. https:/doi.org/10.1016/j.chemgeo.2018.09.011

Marynowski, L., Zaton, M., Rakocinski, M., Filipiak, P., Kurkiewicz, S., Pearce, T.J., 2012. Deciphering the upper Famennian Hangenberg Black Shale depositional environments based on multi-proxy record. Palaeogeography, Palaeoclimatology, Palaeoecology 346, 66–86.

Masse, J.P., Bellion, Y., Benkhelil, J., Boulin, J., Cornee, J.J., Dercourt, J., Guiraud, R., Mascle, G., Poisson, A., Ricou, L.E., Sandulescu, M., 1993. Lower Aptian palaeoenvironments 114–112 Ma. In: Dercourt, J., et al. (Eds.), Atlas Tethys Palaeoenvironmental Maps, Maps Beceip-Franlab, Rueil-Malmaison.

Méhay, S., Keller, C.E., Bernasconi, S.M., Weissert, H., Erba, E., Bottini, C., Hochuli, P.A., 2009. A volcanic CO_2 pulse triggered the Cretaceous Oceanic Anoxic Event 1a and a biocalcification crisis. Geology 37, 819–822.

Menegatti, A.P., Weissert, H., Brown, R.S., Tyson, R.V., Farrimond, P., Strasser, A., Caron, M., 1998. High-resolution $\delta^{13}C$ stratigraphy through the Early Aptian "Livello Selli" of the Alpine Tethys. Paleoceanography 13, 530–545.

Millán, M.I., Weissert, H., Fernández-Mendiola, P.A., García-Mondéjar, J., 2009. Impact of Early Aptian carbon cycle perturbations on evolution of a marine shelf system in the Basque-Cantabrian Basin (Aralar, N Spain). Earth Planet. Sci. Lett. 287, 392–401.

Millán, M.I., Weissert, H.J., López-Horgue, M.A., 2014. Expression of the late Aptian cold snaps and the OAE1b in a highly subsiding carbonate platform (Aralar, northern Spain). Palaeogeography, Palaeoclimatology, Palaeoecology, 167–179.

Millán, M.I., Weissert, H.J., Owen, H., Fernández-Mendiola, P.A., and García-Mondéjar, J., 2011. The Madotz Urgonian platform (Aralar, northern Spain): Paleoecological changes in response to Early Aptian global environmental events. Palaeogeography, Palaeoclimatology, Palaeoecology 312, 167–180.

1021 Moldovan, J.M., Seifert, W.K., Gallegos, E.J., 1985. Relationship between petroleum composition and depositional
1022 environment of petroleum source rocks. American Association of Petroleum Geologists Bulletin 69, 1255–1268.
1023 Molina, J.M., 1987. Análisis de facies del Mesozoico en el Subbético Externo. (Prov. de Córdoba y sur de Jaén). PhD thesis,
1024 Universidad de Granada, Granada, 512 pp.
1025 Molina, J.M., Hernández-Molina, F.J., 1993. Concreciones de barita en el Cretácico (Aptiense–Albiense) del Subbético
1026 (Cordilleras Béticas). Boletín Geológico y Minero 104, 548–573.
1027 Monteiro, F.M., Pancost, R.D., Ridgwell, A., Donnadieu, Y. 2012. Nutrients as the dominant control on the spread of anoxia
1028 and euxinia across the Cenomanian-Turonian oceanic anoxic event (OAE2): Model-data comparison.
1029 Paleoceanography, 27, art. no. PA4209. DOI: 10.1029/2012PA002351
1030 Moreno-Bedmar, J.A., Company, M., Sandoval, J., Tavera, J.M., Bover-Arnal, T., Salas, R., Delanoy, G., Maurrasse, F.J.M.R.,
1031 Martínez, R., 2012. Lower Aptian ammonite and carbon isotope stratigraphy in the eastern Prebetic Domain (Betic
1032 Cordillera, southeastern Spain). Geologica Acta 10, 333–350.
1033 Moullade, M., Tronchetti, G., Granier, B., Bornemann, A., Kuhnt, W., Lorenzen, J., 2015. High-resolution integrated
1034 stratigraphy of the OAE1a and enclosing strata from core drillings in the Bedoulian stratotype (Roquefort-La
1035 Bédoule, SE France). Cretaceous Research 56, 119–140.
1036 Mutterlose, J., Bottini, C., 2013. Early Cretaceous chalks from the North Sea giving evidence for global change. Nature
1037 Communications. https:/doi.org/10.1038/ncomms2698
1038 Mutterlose, J., Bottini, C., Schouten, S., Sinninghe-Damsté, J.S., 2014. High sea-surface temperatures during the early
1039 Aptian Oceanic Anoxic Event 1a in the Boreal Realm. Geology 42, 439-442.
1040 Naafs, B.D.A., Castro, J.M., De Gea, G.A., Quijano, M.L., Schmidt, D.N., and Pancost, R.D., 2016, Gradual and sustained
1041 carbon dioxide release during Aptian Oceanic Anoxic Event 1a: Nature Geoscience. doi: 10 .1038 /ngeo2627.
1042 Naafs, B.D.A., Pancost, R.D., 2016. Sea-surface temperature evolution across Aptian Oceanic Anoxic Event 1a. Geology 44.
1043 https:/doi.org/10.1130/G38575.1
1044 Najarro, M., Rosales, I., Moreno-Bedmar, J.A., Gea, G.A. de, Barrón, E., Company, M., Delanoy, G., 2011. High-resolution
1045 chemo- and biostratigraphic records of the Early Aptian oceanic anoxic event in Cantabria (N Spain):
1046 Palaeoceanographic and palaeoclimatic implications. Palaeogeography, Palaeoclimatology, Palaeoecology 299,
1047 137–158.
1048 Newman, D.K., Neubauer, J., Ricci, J.N., Wu, C.H., Pearson, A., 2016. Cellular and Molecular Biological Approaches to
1049 Interpreting Ancient Biomarkers. Annual Review of Earth and Planetary Sciences 44, 493–522-

1050 Niebuhr, B., 2005. Geochemistry and time-series analyses of orbitally forced Upper Cretaceous marlelimestone rhythmites
1051 (Lehrte West Syncline, northern Germany). Geological Magazine 142, 31-55.

1052 Nijenhuis, I.A., Becker, J., De Lange, G.J., 2001. Geochemistry of coeval marine sediments in Mediterranean ODP cores and
1053 a land section: implications for sapropel formation models. Palaeogeography, Palaeoclimatology, Palaeoecology
1054 165, 97-112.

1055 Nuñez-Useche, F., Barragán, R., Moreno-Bedmar, J.A., Canet, C., 2015. Geochemical and paleoenvironmental record of the
1056 early to early late Aptian major episodes of accelerated change: Evidence from Sierra del Rosario, Northeast
1057 Mexico. Sedimentary Geology 324, 47–66.

1058 O'Dogherty, L., 1994. Biochronology and Paleontology of mid-Cretaceous radiolarians from northern Apennines (Italy) and
1059 Betic Cordillera (Spain). PhD thesis, Institut de Géologie et Paléontologie, University of Lausanne, 413 pp.

1060 O'Dogherty, L., Aguado, R., de Gea, G.A., Sandoval, J., 2011. Registro isotópico del evento anóxico oceánico del Aptiense
1061 Inferior (OAE1a) en radiolaritas del Subbético. Paleontologia i Evolució Memòria especial 5, 273–275.

1062 Olivet, J.M., 1996. La cinématique de la plaque ibérique. Bulletin des Centres de Recherches Exploration-Production Elf-
1063 Aquitaine 20, 131–195.

1064 Ourisson, G., Albrecht, P., Rohmer, M., 1982. Predictive microbial biochemistry from molecular fossils to prokaryotic
1065 membranes. Trends in Biochemical Sciences 7, 236–239.

1066 Paschal, O., Carmichael, S.K., Königshof, P., Waters, J.A., Ta, P.H. Komatsu, T., Dombrowski, A., 2019. The Devonian-
1067 Carboniferous boundary in Vietnam: Sustained ocean anoxia with a volcanic trigger for the Hangenberg Crisis?.
1068 Global and Planetary Change 175, 64–81. https://doi.org/10.1016/j.gloplacha.2019.01.02

1069 Pedersen, T.F., Calvert, S.E., 1990. Anoxia vs. productivity: what controls the formation of organic-carbon-rich sediments
1070 and sedimentary rocks. American Association of Petroleum Geologists Bulletin 74, 454–466.

1071 Peters, K.E., Moldowan, J.M., 1991. Effects of source, thermal maturity, and biodegradation on the distribution and
1072 isomerization of homohopanes in petroleum. Organic Geochemistry 17, 47–51.

1073 Peters, K.E., Walters, C.C., Moldowan, J.M., 2005. 2nd ed. The Biomarker Guide. Cambridge University Press (1155pp.).

1074 Polteau, S., Hendriks, B.W.H., Planke, S., Ganerød, M., Corfu, F., Faleide, J.I., Midtkandal, I., Svensen, H.S., Myklebust, R.,
1075 2016. The Early Cretaceous Barents Sea Sill Complex: Distribution, 40Ar/39Ar geochronology, and implications for
1076 carbon gas formation. Palaeogeography, Palaeoclimatology, Palaeoecology 441, 83-95. https:/doi.org/
1077 10.1016/j.palaeo.2015.07.007

Price, G.D., 2003. New constraints upon isotope variation during the early Cretaceous (Barremian–Cenomanian) from the Pacific Ocean. Geological Magazine 140, 513–522.

Quijano, M.L., Castro, J.M., Pancost, R.D., Gea, G.A. de, Najarro, M., Aguado, R., Rosales, I., Martín-Chivelet, J., 2012. Organic geochemistry, stable isotopes, and facies analysis of the Early Aptian OAE – New records from Spain (Western Tethys). Palaeogeography, Palaeoclimatology, Palaeoecology 365-366, 276–293.

Rashby, S.E., Sessions, A.L., Summons, R.E., Newman, D.K., 2007. Biosynthesis of 2-methylbacteriohopanepolyols by an anoxygenic phototroph. PNAS 104:15099–104.

Redfield, A.C., 1958. The biological control of chemical factors in the environment. American Scientist 46, 205–221.

Renard, M., Rafélis, M., de Emmanuel, L., Moullade, M., Masse, J.P., Kuhnt, W., Bergren, J.A., Tronchetti, G., 2005. Early Aptian $\delta^{13}C$ and manganese anomalies from the historical Cassis-La-Bédoule stratotype sections (S.E. France): relationship with methane hydrate dissociation event and stratigraphic implications. Carnets de Géologie 1 (8) (Brest, Article 2005/04 (CG2005_A04)).

Ricci, J.N., Morton, R., Kulkarni, G., Summers, M.L., Newman, D.K., 2016. Hopanoids play a role in stress tolerance and nutrient storage in the cyanobacterium Nostoc punctiforme. Geobiology, 15 (1), pp. 173-183. https:/doi.org/10.1111/gbi.12204

Robinson, S.A., Heimhofer, U., Hesselbo, S.P., Petrizzo, M.R., 2017. Mesozoic climates and oceans – a tribute to Hugh Jenkyns and Helmut Weissert. *Sedimentology* 64, 1-15, doi: 10.1111/sed.12349

Robinson, S.A., Williams, T., Bown, P.R. 2004. Fluctuations in biosiliceous production and the generation of Early Cretaceous oceanic anoxic events in the Pacific Ocean (Shatsky Rise, Ocean Drilling Program Leg 198). Paleoceanography, 1-19. https:/doi.org/10.1029/2004PA001010

Roth, P.H., 1978. Cretaceous nannoplankton biostratigraphy and oceanography of the northwestern Atlantic ocean. Initial Reports of the Deep Sea Drilling Project 44, 731–759.

Ruiz-Ortiz, P.A., 1980. Análisis de facies del Mesozoico de las Unidades Intermedias (entre Castril—provincia de Granada—y Jaén). Ph.D. Thesis. University of Granada, 372 pp.

Ruiz-Ortiz, P.A., Molina, J.M., Nieto, L.M., Castro, J.M., de Gea, G., 2001. Itinerarios geológicos por el Mesozoico de la provincia de Jaén. 1. Introducción al Mesozoico de la parte externa del paleomargen sudibérico. Cordillera Bética: IV Coloquio del Cretácico de España, University of Jaén, pp. 11–24.

1105 Sánchez-Hernández, Y., Maurrasse, F., 2016. The influence of regional factors in the expression of oceanic anoxic event 1a
1106 (OAE1a) in the semi-restricted Organyà Basin, south-central Pyrenees, Spain. Palaeogeography,
1107 Palaeoclimatology, Palaeoecology 441, 582–598.
1108 Sanz de Galdeano, C., 1973. Geología de la transversal Jaén-Frailes. PhD thesis, Universidad de Granada, Granada, 274 pp.
1109 Schlanger, S.O., Jenkyns, H.C., 1976. Cretaceous oceanic anoxic events: causes and consequences. Geologie en Mijnbouw
1110 55, 179–184.
1111 Schoepfer, S.D., Shen, J. Wei, H., Tyson, R.V., Ingall, E., Algeo, T.J., 2015. Total organic carbon, organic phosphorus, and
1112 biogenic barium fluxes as proxies for paleomarine productivity. Earth Science Reviews 149, 19-48.
1113 Seifert, W.K., Moldowan, J.M., 1980. The effect of thermal stress on source-rock quality as measured by hopane
1114 stereochemistry. Physics and Chemistry of the Earth 12, 229–237.
1115 Sinninghé-Damsté, J.P., Kenig, F., Koopmans, M.P., Koster, J.G., Schouten, S., Hayes, J.M., De Leeuw, J.W., 1995. Evidence
1116 for gammacerane as an indicator of water column stratification. Geochimica et Cosmochimica Acta 59, 1895–
1117 1900.
1118 Skelton, P.W. (Ed.), 2003. The Cretaceous World. The Open University, Milton Keynes, and Cambridge University Press,
1119 Cambridge (360pp.).
1120 Skelton, P.W., Castro, J.M., Ruiz-Ortiz, P.A. 2019. Aptian carbonate platform development in the Southern Iberian
1121 Palaeomargin (Prebetic of Alicante, SE Spain). BSGF – Earth Sciences Bulletin 190 (2019) 3.
1122 https://doi.org/10.1051/bsgf/2019001
1123 Stein, M., Föllmi, K.B., Westermann, S., Godet, A., Adatte, T., Matera, V., Fleitmann, D., Berner, Z., 2011. Progressive
1124 palaeoenvironmental change during the Late Barremian–Early Aptian as prelude to Oceanic Anoxic Event 1a:
1125 Evidence from the Gorgo a Cerbara section (Umbria-Marche basin, central Italy). Palaeogeography,
1126 Palaeoclimatology, Palaeoecology 302, 396–406.
1127 Stein, M., Westermann, S., Adatte, T., Matera, V., Fleitmann, D., Spangenberg, J.E., Föllmi, K.B.2012. Late Barremian-Early
1128 Aptian palaeoenvironmental change: The Cassis-La Bédoule section, southeast France. Cretaceous Research, 37,
1129 209-222. https:/doi.org/10.1016/j.cretres.2012.03.021
1130 Summons, R. E., Jahnke, L. L., Hope, J. M., Logan, G. A., 1999. 2-Methylhopanoids as biomarkers for cyanobacterial oxygenic
1131 photosynthesis. Nature 400, 554– 557.

1132 Tejada, M.L., Suzuki, K., Kuroda, J., Coccioni, R., Mahoney, J.J., Ohkouchi, N., Sakamoto, N., Tatsumi, Y., 2009. Ontong Java
1133 Plateau eruption as a trigger for the early Aptian oceanic anoxic event. Geology 37, 855–858.
1134 Tribovillard N., Algeo T. J., Lyons T. W., Riboulleau A., 2006. Trace metals as paleoredox and paleoproductivity proxies: an
1135 update. Chemical Geology 232, 12–32.
1136 Turgeon, S.C., Brumsack, H.J., 2006. Anoxic vs dysoxic events reflected in sediment geochemistry during the Cenomanian-
1137 Turonian Boundary Event (Cretaceous) in the Umbria-Marche Basin of central Italy. Chemical Geology 234, 321-
1138 339.

1139 Tyson, R.V., 2001. Sedimentation rate, dilution, preservation, and total organic carbon: some results of a modeling study.
1140 Organic Geochemistry 32, 333–339.

1141 Tyson, R.V., 2005. The "productivity versus preservation" controversy; cause, flaws, and resolution. In: Harris, N.B. (Ed.),
1142 Deposition of Organic-carbon-rich Sediments Models, Mechanisms, and Consequences. Society for Sedimentary
1143 Geology (SEPM- SSG) Special Publication 82, pp. 17–33.

1144 van Breugel, Y., Schouten, S., Tsikos, H., Erba, E., Price, G.D., Sinninghe Damsté, J.S., 2007. Synchronous negative carbon
1145 isotope shifts in marine and terrestrial biomarkers at the onset of the early Aptian oceanic anoxic event 1a:
1146 Evidence for the release of ^{13}C-depleted carbon into the atmosphere. Paleoceanography 22, PA1210. doi:
1147 10.1029/2006pa001341.
1148 Vera, J.A., 1988. Evolución de los sistemas de depósito en el margen ibérico de la Cordillera Bética. Revista Sociedad
1149 Geológica España 1, 373–391.
1150 Vera, J.A., 2004. Cordillera Bética y Baleares. In: Vera, J.A. (Ed.), Geología de España. Sociedad Geológica de España e
1151 Instituto Geológico y Minero de España, Madrid, pp. 345–464.
1152 Vergès, J., García-Senz, J., 2001. Mesozoic evolution and Cainozoic inversion of the Pyrenean Rift. In: Ziegler, P.A., Cavazza,
1153 W., Robertson, A.H.F., Crasquin-Soleau, J. (Eds.), Peri-Tethys Memoir 6: Peri-Tethyan Rift/Wrench Basins and
1154 Passive Margins: Mémoires du Muséum National d'Historie Naturelle, Paris, 186, pp. 187–212.
1155 Vilas, L., Martín-Chivelet, J., Arias, C., 2003. Integration of subsidence and sequence stratigraphic analyses in the Cretaceous
1156 carbonate platforms of the Prebetic (Jumilla-Yecla Region), Spain. Palaeogeography Palaeoclimatology
1157 Palaeoecology 200, 107–129.
1158 Volkman, J. K., Barrett, S. M., Blackburn, S. I., Man- Sour, M. P., Sikes, E. L., Gelin, F., 1998. Microalgal biomarkers: a review
1159 of recent research developments. Organic Geochemistry 29, 1163–1179.

1160 Waples, D.W., Machihara, T., 1991. Biomarkers for geologists. American Association of Petroleum Geologists—Methods in
1161 Exploration Series, 9 (91pp.).
1162 Warning, B., Brumsack, H.J., 2000. Trace metal signatures of eastern Mediterranean sapropels. Palaeogeography,
1163 Palaeoclimatology, Palaeoecology 158, 293-309.
1164 Wedepohl, K.H., 1991. The composition of the upper Earth's crust and the natural cycles of selected metals. Metals in
1165 natural raw materials. Natural resources. In: Merian, E. (Ed.), Metals and Their Compounds in the Environment.
1166 VCH, Weinheim, pp. 3–17.
1167 Weissert, H., 1990. Siliciclastics in the Early Cretaceous Tethys and North Atlantic oceans: documents of periodic
1168 greenhouse climate conditions. Mem. Soc. Geol. Ital. 44, 59–69.
1169 Weissert, H., Erba, E., 2004. Volcanism, CO_2 and palaeoclimate: a Late Jurassic–Early Cretaceous carbon and oxygen isotope
1170 record. Journal of the Geological Society, London 161, 1–8.
1171 Welander, P.V., Coleman, M.L., Sessions, A.L., Summons, R.E., Newman, D.K., 2010. Identification of a methylase required
1172 for 2-methylhopanoid production and implications for the interpretation of sedimentary hopanes. Proceedings of
1173 the National Academy of Sciences 107, 8537-8542. https:/doi.org/10.1073/pnas.0912949107
1174 Westermann, S., Föllmi, K.B., Adatte, T., Matera, V., Schnyder, J., Fleitmann, D., Fiet, N., Ploch, I., Duchamp-Alphonse, S.,
1175 2010. The Valanginian $d^{13}C$ excursion may not be an expression of a global anoxic event. Earth and Planetary
1176 Science Letters 290, 118-131.
1177 Westermann, S., Stein, M., Matera, V., Fiet, N., Fleitmann, D., Adatte, T., Föllmi, K.B., 2013. Rapid changes in the redox
1178 conditions of the western Tethys Ocean during the early Aptian oceanic anoxic event: Geochimica et
1179 Cosmochimica Acta 121, 467–486.
1180 Westermann, S., Vance, D., Cameron, V., Archer, C., Robinson, S.A., 2014. Heterogeneous oxygenation states in the Atlantic
1181 and Tethys oceans during Oceanic Anoxic Event 2. Earth and Planetary Science Letters 404, 178-189.
1182 https:/doi.org/ 10.1016/j.epsl.2014.07.018
1183 Xie, S., Pancost, R.D., Yin, H., Wang, H., Evershed, R.P. 2005. Two episodes of microbial change coupled with Permo/Triassic
1184 faunal mass extinction. Nature, 434, 494-497. https:/doi.org/10.1038/nature03396
1185 Xu, W., Ruhl, M., Jenkyns, H.C., Hesselbo, S.P., Riding, J.B., Selby, D., Naafs, B.D.A., Weijers, J.W.H., Pancost, R.D., Tegelaar,
1186 E.W., Idiz, E.F., 2017. Carbon sequestration in an expanded lake system during the Toarcian oceanic anoxic event.
1187 *Nature Geoscience* 10, 129-134. https:/doi.org/10.1038/ngeo2871

1188 Yamamoto, K., Ishibashi, M., Takayanagi, H., Asahara, Y., Sato, T., Nishi, H., Iryu, Y. 2013. Early Aptian paleoenvironmental
1189 evolution of the Bab Basin at the southern Neo-Tethys margin: Response to global carbon-cycle perturbations
1190 across Ocean Anoxic Event 1a. Geochemistry, Geophysics, Geosystems, 14, 1104-1130.
1191 https:/doi.org/10.1002/ggge.20083
1192 Ziegler, P.A., 1988. Evolution of the Artic–North Atlantic and the Western Tethys, publ. Int. lithos. Program, 0144. AAPG
1193 Memoir 43 (193pp.)